The DOI for this manuscript is doi: 10.1175/JCLI-D-18-0159.1

The final published version of this manuscript will replace the preliminary version at the above DOI once it is available.

If you would like to cite this EOR in a separate work, please use the following full citation:

Singh, D., R. Seager, B. Cook, M. Cane, M. Ting, E. Cook, and M. Davis, 2018: Climate and the Global Famine of 1876-78. J. Climate. doi:10.1175/JCLI-D-18-0159.1, in press.

Climate and the Global Famine of 1876-78

Deepti Singh[1,2*], Richard Seager[2], [2,3]Benjamin I. Cook, Mark Cane[2], Mingfang Ting[2], Edward Cook[2], and Michael Davis[4]

[1]School of the Environment, Washington State University, Vancouver, WA

[2]Lamont-Doherty Earth Observatory, Columbia University, Palisades, NY

[3]NASA Goddard Institute for Space Studies, New York, NY

[4]University of California, Riverside, CA

* corresponding author: Deepti Singh

Email: deepti.singh@wsu.edu

Phone: 650-468-8791

Address: School of the Environment

14204 NE Salmon Creek Avenue,

Vancouver, WA-98686

Keywords: natural climate variability, multi-year drought, El-Niño, climate impacts

Abstract

From 1875-78, concurrent multi-year droughts in Asia, Brazil, and Africa, referred to as the Great Drought, caused widespread crop failures, catalyzing the Global Famine, which had fatalities exceeding 50 million people and long-lasting societal consequences. Observations, paleoclimate reconstructions, and climate model simulations are used to 1) demonstrate the severity and characterize the evolution of drought across different regions, and 2) investigate the underlying mechanisms driving its multi-year persistence. Severe or record-setting droughts occurred on continents in both hemispheres and in multiple seasons, with Monsoon Asia the hardest hit, which experienced the single most intense and the second most expansive drought in the last 800 years. The extreme severity, duration, and extent of this global event is associated with an extraordinary combination of preceding cool tropical Pacific conditions (1870-76), a record breaking El Niño (1877-78), record strong Indian Ocean Dipole (1877) and record warm North Atlantic Ocean (1878) conditions. Composites of historical analogues and two sets of ensemble simulations – one forced with global sea-surface temperatures (SSTs) and another forced with tropical Pacific SSTs - were used to distinguish the role of the extreme conditions in different ocean basins. While the drought in most regions was largely driven by the tropical Pacific SST conditions, an extreme positive phase of the Indian Ocean Dipole and warm North Atlantic SSTs, both likely aided by the strong El Niño in 1877-78, intensified and prolonged droughts in Brazil and Australia respectively and extended the impact to northern and southeastern Africa. Climatic conditions that caused the Great Drought and Global Famine arose from natural variability, and their recurrence, with hydrological impacts intensified by global warming, could again potentially undermine global food security.

1. Introduction

During the late 19th century, a series of famines affected vast parts of Asia, causing mortality on a scale that would be unthinkable today (Davis 2001). Of these, the Global Famine lasting from 1876-1878 was the most severe and widespread in at least the past 150 years (Hasell and Roser 2017; Gráda 2009; Davis 2001). The Global Famine inflicted acute distress upon populations in diverse parts of South and East Asia, Brazil and Africa, with total human fatalities likely exceeding 50 million. These famines were associated with prolonged droughts in India, China, Egypt, Morocco, Ethiopia, southern Africa, Brazil, Colombia, and Venezuela (Davis 2001; Clarke 1878; Hunter 1877). Historical documentation indicates famine-related mortality between 12.2-29.3 million in India, 19.5-30 million in China, and ~2 million in Brazil (Davis 2001), amounting to ~3% of the global population at the time. It was arguably the worst environmental disaster to ever befall humanity and one of the worst calamities of any sort in at least the last 150 years, with the loss of life comparable to the World Wars and the Influenza epidemic of 1918-19. The triggers for the famine were acute droughts, but political-economic factors, especially the neglect or destruction of traditional systems of water and grain storage, were responsible for translating crop failure into unprecedented mass mortality (Davis 2001).

Studies published in *Nature* in 1877-78 proposed weakened sun-spot activity as the primary cause of the drought over India (Buchan 1877; Derby 1878; Hunter 1877), though this was soon questioned (Blanford 1887). Only a few modern studies have analyzed the character, dynamics and causes of the drought conditions and only in some regions during the Global Famine (Hao et al. 2010; Aceituno et al. 2008; Kang et al. 2013). *Zhixin et al. (2010)* showed that the 1876-78 drought in northern China, which resulted in consecutive crop failures, was the most severe in the last 300 years based on seasonal precipitation reconstructions over the Yellow River basin. *Aceituno et al. (2009)* showed that northeastern Brazil experienced severe dry conditions, and parts of the northwestern coastal regions and southeastern South America experienced intense rainfall and frequent flooding during the 1877-78 period. These studies ascribed these extremes to El Niño-like conditions in the Pacific (Aceituno et al. 2008; Hao et al. 2010; Kiladis and Diaz 1986), as did *Davis (2001)*, which *Kiladis and Diaz (1986)* found to be comparable in magnitude to the strong 1982-83 El Niño but with stronger global impacts. To the best of our knowledge, there appears to be no prior global-scale analysis and attribution of the causes of the drought in the years before, during and after the 1877-78 El Niño.

In this study, we detail the characteristics and causes of the multi-year global drought associated with the Great Famine, herein referred to as the Great Drought, with new datasets of hydroclimate and sea-surface temperatures (SST). We combine drought estimates from four, widely-used tree-ring based regional drought atlases (Cook et al. 2010a, 2015, 2007; Palmer et al. 2015) and rain-gauge data from the Global Historical Climatology Network (GHCN) (Lawrimore et al. 2011) to characterize the spatial and temporal features of the Great Drought and contextualize these features within the ~ 140-year instrumental record and ~800-year paleoclimate record. The drought atlases provide an annually-resolved estimation of hydroclimatic conditions, while the rain-gauge data include regions not covered in the drought atlases and facilitate an examination of the seasonal evolution of rainfall anomalies and potential climatic drivers. With the further aid of SST datasets and climate model simulations, we identify the climatic conditions that shaped this dramatic multi-year event across different regions, including conditions preceding, during and following the outsized El Niño event, that extended the duration and severity of the Great Drought in regions bordering the Atlantic and Indian

Oceans. An understanding of the characteristics and causes of this event is the first step towards predicting the occurrence and impacts of similarly widespread and prolonged droughts, and their consequent impacts on food security.

2. Materials and Methods

2.1. Hydroclimate data:

To characterize the hydro-climatic conditions of the Great Drought, we employ instrumental records of precipitation and tree-ring based drought atlases. Monthly rainfall data for land-based stations is from the extensive GHCN database (Lawrimore et al. 2011), which archives data for over 20,000 stations from multiple sources around the world. The area-weighted average monthly rainfall for Indian sub-regions and for the All-India domain are from the Indian Institute of Tropical Meteorology (IITM) (Parthasarathy et al. 1995, 1993, 1994, 1987), and are constructed from a uniformly distributed network of 306 stations across India with data availability from 1871-2014. IITM defines these sub-regions based on the similarity in their rainfall characteristics (refer Fig. 2 in (Parthasarathy et al. 1995) for a map of the sub-regions). Rainfall for Fortaleza, Brazil (3.4°S, 38.3°W) was accessed from the Joint Institute for the Study of Atmosphere and Oceans, University of Washington (JISAO). Rainfall for Shanghai, China (31.4°N, 121.47°E) and 6 stations (Durban, Brakfontein, Graaf Reinet, SomersetEast, Grahamstown, and Port Elizabeth) in the Eastern Cape and KwaZulu-Natal provinces in South Africa, were extracted from the GHCN database. The stations in the Eastern Cape-Natal region in South Africa were chosen based on the availability of data for all years between 1875-1997. For most of these stations, the GHCN records ended in 1997.

In addition to these direct rainfall records, we analyze tree ring-based reconstructions of the Palmer Drought Severity Index (PDSI) from four gridded drought atlases - Monsoon-Asia Drought Atlas version 2 (MADA; 1°x1°)(Cook et al. 2010a), Old World Drought Atlas (OWDA; 0.5°x0.5°)(Cook et al. 2015), North American Drought Atlas (NADA; 0.5°x0.5°)(Cook et al. 2010b), and the eastern Australia and New Zealand Drought Atlas (ANZDA; 0.5°x0.5°)(Palmer et al. 2015). These atlases extend the current instrumental record to provide seasonal-scale hydroclimate information back to 1500 C.E. in the ANZDA and 1200 C.E. or longer in the northern hemisphere drought atlases. The northern hemisphere drought atlases provide gridded reconstructions of the boreal summer (June-August) PDSI, whereas the ANZDA reflects the austral summer (December-February) PDSI. PDSI is a widely used measure of the severity of surface wetness or dryness. The severity of dry conditions based on PDSI values are typically classified as abnormally dry (-1.0 to -1.9), moderate drought (-2.0 to -2.9), severe drought (-3.0 to -3.9), extreme drought (-4.0 to -4.9), and exceptional drought (<-5.0). A similar classification holds for wet conditions.

PDSI integrates moisture supply (i.e precipitation) and demand (i.e evapotranspiration) over a year or more and therefore the seasonal PDSI contains hydroclimate information from the preceding seasons (Cook et al. 2010a, 2015, 2007). For example, the reconstructed June-August PDSI values in the western U.S. are strongly influenced by precipitation and temperature in the preceding winter, during which the region typically receives the largest fraction of precipitation (Baek et al. 2017). These properties of PDSI also help explain why there is not always a one-to-one relationship between rainfall and the drought atlases used here, e.g. over India, Europe and eastern Australia. It should be noted that few tree ring chronologies from India go into the MADA. The MADA tends to underestimate the overall severity of the droughts in India as indicated by the rainfall data. The complexity of the rainfall patterns over India coupled with the somewhat sparse tree-ring network used to produce the MADA over India (Cook 2015; Cook et al. 2010a) probably contribute to this apparent disparity. However, reconstructed drought in 1877 over Northeast and Peninsular India match the instrumental data reasonably well. This further supports the use of the MADA here to complement the extensive rain gauge network that covers the drought period. In the text, we refer to Monsoon Asia as the domain covered by the MADA.

2.2. Climate Indices and SST data:

We use monthly time series of sea-level pressure (SLP) at the Madras Observatory in India (1796-2000)(Allan et al. 2002), the Niño 1.2, 3,3.4, and 4 Indices (1870-present) (Trenberth and Stepaniak 2001), the Atlantic Multi-decadal Oscillation Index (Enfield et al. 2001) (AMO;1871-present) from the National Oceanic and Atmospheric Administration Earth System Research Observatory’s Physical Climate Division (NOAA ESRL PSD) database. The Niño Indices are area-weighted averages of the SST anomalies relative to the 1901-1950 mean over the Niño 1+2 (0-10°S and 90-80°W), Niño 3 (5°S-5°N and 150-90°W), Niño 3.4 (5°S-5°N and 170-120°W), and Niño 4 (5°S-5°N and 160°E-150°W) regions. The AMO Index is the unsmoothed, de-trended, area-weighted average SST over the North Atlantic (0-70°N). In addition, we use the monthly, SLP record from Darwin, Australia (1866-present) that is closely related to the Southern Oscillation Index (SOI), a measure of the pressure difference between Darwin and Tahiti stations and an indicator of the large-scale El Niño Southern Oscillation (ENSO) variability (Trenberth 1984; Trenberth and NCAR Staff 2016). Trenberth and NCAR Staff (2016) recommend using the Darwin SLP instead of the SOI index due to the lack of reliability of the Tahiti record prior to 1935. To represent the Indian Ocean Dipole (IOD), we use the monthly Dipole Mode Index (DMI; 1856-present), calculated as the SST difference between the western (50-70°E and 10°S-10°N) and eastern (90-110°E and 10°S-0°N) equatorial Indian Ocean (Saji 2003), which is available from the Japan Agency for Marine-Earth Science and Technology.

Global, monthly SSTs are from the Extended Reconstructed Sea Surface Temperature (ERSST) dataset version 5, which is available at a 2°x2° spatial resolution (Huang et al. 2014). In addition, Hadley Centre Global Sea Ice and Sea Surface Temperature (HADISST) version 1.1 (Rayner et al. 2003) and Kaplan Extended SST version 2 (Kaplan et al. 1998; Reynolds and Smith 1994) are used to quantify the uncertainty in the SST-derived Niño indices. Gridded precipitation data (0.5°x0.5°) for 1900-present are from the Climatic Research Unit (CRU) dataset version 4.01 (Harris et al. 2014).

Globally gridded (2°x2°) surface temperature, humidity, sea-level pressure, and precipitation are from the 56-member NOAA-CIRES Twentieth Century Reanalysis Project version 2c (20CR). In addition to the monthly means, the variability in the 20CR ensemble for each variable is quantified using the standard deviations between the 56-members. A comprehensive analysis of the performance of 20CR precipitation against observations and other reanalysis products is provided in Lee and Biasutti (2014), where it is shown that 20CR better represents rainfall over tropical land and is comparable to other reanalyses over the midlatitudes. Relevant to this study, we compare the climatology of 20CR precipitation and teleconnection patterns with CRU (Fig. S1). The main climatological features of precipitation and its correlations with the Nino 3.4, AMO and DMI indices in 20CR are similar to CRU. The strength of precipitation-Nino3.4 correlations are weaker over South Asia, precipitation-AMO correlations are weaker over the Mediterranean and stronger over southern Africa, and precipitation-DMI correlations are weaker over Australia in 20CR relative to CRU. However, the sign of these correlations is consistent across all regions relevant to this study.

2.3. Drought Characteristics:

To evaluate the long-term context of the hydroclimate conditions over Asia during the three years of the Great Drought, we characterize the spatial extent and severity of drought for each year in the MADA. The spatial extent of the drought is defined as the fractional area of this domain with abnormally dry conditions (i.e PDSI $\leq$-1.0). The drought severity is the area-weighted average PDSI over the entire domain. We limit our analysis to post 1200 C.E. during which there is spatial coverage of PDSI across the entire MADA domain (~10°S-60°N, 65-150°E) for consistency.

2.4. ENSO Characteristics:

In this study, we characterize El Niños based on the area-weighted average SST anomalies over the Niño3.4 region (Barnston et al. 1997). We examine the intensity and duration of historical El Niño events to understand their differing impacts. Their duration is defined as the number of consecutive months with SST anomalies over the Niño 3.4 region exceeding 0.5°C, following the NOAA Climate Prediction Center threshold. Their cumulative intensity is defined as the sum of the monthly Niño 3.4 SST anomalies over the entire duration of the event. This metric is a combined measure of the strength and duration of an event, both of which are important for interpreting its regional impacts.

2.5. Climate Model Experiments

We use an ensemble of SST-forced simulations (1856-2016) with the atmospheric component of the NCAR CCM3 to examine the role of the tropical Pacific SST conditions relative to global

SST conditions in shaping this multi-year drought. The first ensemble of simulations involves lower boundary forcing from the observed global SSTs and are referred to as the Global Ocean-Global Atmosphere (GOGA) simulations. SSTs for these simulations are blended from the Kaplan dataset (Kaplan et al. 1998) used in the tropical Pacific (20°N-20°S) and the Met Office Hadley Centre's sea ice and sea surface temperature (SST) data set (Rayner et al. 2003) used outside of the tropical Pacific. The second ensemble of simulations referred to as the Pacific Ocean Global Atmosphere-Mixed Layer (POGA-ML) only specifies SSTs in the tropical Pacific from the Kaplan dataset and SST anomalies in other regions are computed using an ocean mixed layer ocean model. Heat exchange between the atmosphere and the ocean occurs at the surface based on the computed energy fluxes from the atmosphere model, allowing SST variations outside the tropical Pacific to be forced by the tropical Pacific SSTs. Therefore, the climate response in the POGA-ML can be driven either directly by the tropical Pacific or by remote SST variations forced by the tropical Pacific. To capture the role of internal atmospheric variability, each ensemble has 16 members with identical boundary forcings that only differ in the initial atmospheric conditions. Additional details of these experiments are described in (Seager et al. 2005).

On comparison with CRU observations for the 1901-1950 baseline period, the CCM3 GOGA simulations capture the main spatial features of the observed annual precipitation climatology over most regions except parts of Asia (Fig. S1a,c). Over South Asia, the model does not simulate the heavy precipitation center over central India and along the Himalayas (Fig. S1a,c). In addition, the model has a wet bias over central China and a dry bias over eastern China. Similarly, teleconnection patterns with the three modes of variability – ENSO, AMO, and IOD are reasonably well represented in the CCM3 GOGA simulations, supporting the use of the model for this study (Fig. S1). Notable biases in regions of relevance to this study include spatially varying biases over South and East Asia in the Niño3.4-precipitation correlations, stronger than observed teleconnections in the AMO-precipitation correlations over Europe, and weaker than observed teleconnections in the DMI-precipitation correlations over Australia.

To examine the precipitation responses associated with tropical Pacific versus global SST conditions, we compute standardized precipitation anomalies for each ensemble member relative to the ensemble average mean precipitation. For each region that experienced drought conditions during the 1876-78 period, we calculate the area-weighted average precipitation anomalies over land during their major rainy seasons. The significance of the differences between the distributions of area-average precipitation anomalies from the two ensembles are calculated using the Kolmogorov-Smirnov statistical test.

All anomalies for observed and modeled quantities are calculated relative to a climatology evaluated over 1901-1950.

3. **Results**

The Global Famine was initiated by severe droughts in several regions that persisted for multiple seasons between 1875-78. In Fig. 1, we identify the temporal evolution of these regional droughts. The drought started in India with a failure of the 1875 winter monsoon season and dry conditions persisted through the summer of 1877. In East Asia, the drought started in spring 1876 and the lack of rainfall persisted through summer 1878. Subsequently, droughts developed in parts of South Africa, northern Africa and northeastern Brazil in following seasons that lasted till at least 1878. Relatively shorter but severe droughts also occurred in western Africa, Southeast Asia and Australia between mid-1877 and 1878. Droughts in most of these regions are often associated with the occurrence of El Niño events (eg: (Kumar et al. 2006; Slingo and Annamalai 2000; Ropelewski and Halpert 1987; Wang et al. 2017; Xu et al. 2004)). While previous studies (Kiladis and Diaz 1986; Aceituno et al. 2008) have identified the presence of a strong El Niño during the Great Drought, the El Niño conditions only developed in 1877 and waned in 1878. However, the drought in key areas afflicted by famines - including India, northeastern Brazil and China - started prior to the development of the El Niño or lasted longer than its duration.

3.1. *Character and Historical Context of the drought*

Parts of India, East Asia, Central Asia, and Southeast Asia simultaneously experienced abnormally dry conditions (PDSI<-1.0) between 1876-78, with the peak spatial extent in 1877 (Fig. 2). East Asia, the region with the highest number of reported famine deaths (Davis 2001), witnessed the most widespread and persistent droughts across all three years. The drought was most extensive in South, Central and East Asia in 1877. In Southeast Asia, the drought was also the most severe and widespread in 1877 and persisted in many regions through 1878. In addition to Asia, moderate to severe (PDSI<-2.0) drought conditions covered much of northern Europe in 1876. In 1877, abnormally dry conditions (PDSI~-1.0) occurred over parts of eastern Australia and severe drought conditions (PDSI<-3.0) occurred over California and the Mediterranean basin including northern Africa and central Europe (Fig. 2b). In 1878, these dry conditions intensified in the Mediterranean Basin. In addition, moderate to severe droughts (PDSI<-2.0) spread across much of Eastern Australia in 1878 while much of the coterminous U.S. experienced severe wet conditions (PDSI>3.0), both typical of El Niño years (Fig. 2c). These regional droughts were associated with substantial SST anomalies in multiple ocean basins. In the tropical Pacific Ocean, cool SSTs in 1875-76 reversed to warm SSTs in 1876-77 that strengthened in 1877-78 (Fig. 2a-c). In the Atlantic Ocean, warm SSTs developed in the subtropics in 1867-77 and expanded into the tropics in 1877-78 (Fig. 2b-c). In the Indian Ocean, warm SST anomalies developed across the western and northern parts of the basin in 1877-78 (Fig. 2c).

To complement the drought atlas estimates and examine regions not covered by them, we analyze cumulative 12-month (September-August) rainfall anomalies at GHCN stations for 1875-76, 1876-77 and 1877-78 (Fig. 3). Rain gauge data from the 19th century need to be treated with caution and coverage is sparse outside of India and parts of Europe and North America. Nonetheless, the GHCN station data largely confirm the regional droughts identified in the drought atlases, identify other droughts in regions not covered in the drought atlases and bring the drought in India into sharp focus. Several stations in peninsular India recorded anomalously low rainfall exceeding -1.5 standard deviations ($<-1.5\sigma$) in 1875-76 (Fig. 3a). These rainfall deficits intensified and spread across India in 1876-1877. Strong rainfall deficits ($<-1.5\sigma$) also occurred in parts of eastern Australia, southern Africa, the Brazilian Nordeste, and southwestern and northeastern U.S., and moderate deficits ($<-1.0\sigma$) at stations in Southeast and East Asia in 1876-77 (Fig. 3b). Strong rainfall deficits ($<-1.5\sigma$) persisted in the Brazilian Nordeste, Mediterranean, southern Africa, and Southeast Asia in the following year (1877-78; Fig 3c). In contrast, rainfall anomalies over the U.S. and western and peninsular India reversed from very dry to very wet in 1877-78 ($>1.5\sigma$). Differences between station-based rainfall estimates and PDSI-based hydroclimatic conditions might exist because of the misalignment between the seasons of PDSI reconstruction and the Sep-August period used for the cumulative rainfall anomalies. Despite that, these station-based measurements, along with the tree-ring based hydroclimatic indicators, demonstrate severe, concurrent droughts across the tropics and sub-tropics that persisted for multiple seasons within this 3-year period, implicating climate anomalies as a trigger for the Global Famine.

To quantify the extreme, record-setting nature of this drought, we examine key instrumental records dating back to the 1870's for the rainy seasons of 4 regions that experienced major economic or political transitions following severe famines during 1876-78 (Fig. 4). Across most of India, the summer (June-September) monsoon season is the dominant source of rainfall but the winter (October-December) monsoon season contributes substantially to total annual rainfall over peninsular India (Rajeevan et al. 2012). Following 4 consecutive years of weak winter-monsoon rains since 1871, rainfall across India was extremely low ($<-1\sigma$) for the 4 consecutive rainy seasons from the 1875 winter season to the 1877 summer season (Fig. 4a-b). Rainfall deficits were extreme in 1876-77 when the October-December rainfall ($\sim-1.5\sigma$), which was the third lowest on record, was followed by the all-time record low summer monsoon rainfall ($\sim-3.1\sigma$) in 1877 (Fig. 4a-b). This record weakest summer monsoon is consistent with the highest SLP ever recorded at the Madras Observatory, which is an indicator of the strength of the monsoon (Allan et al. 2002) (Fig. 4c). There is limited station availability in China but Shanghai falls within the region of persistent drought (Fig. 2). Though summer is the main rainy season, rainfall in northeastern China starts in spring and El Niño impacts are found to extend across spring and fall seasons (Wang et al. 2017). Shanghai, had below normal rainfall in spring through fall (March-November) between 1876-78 in Shanghai. With rainfall anomalies below -2σ in 1876 and below -1.0σ in 1877, 1876-77 in Shanghai was the lowest 2-year average on record. At Fortaleza in the Brazilian Nordeste, where the main rainfall season is February-May (Polzin and Hastenrath 2014), rainfall was at least 1.5σ below normal for 3 consecutive rainy seasons during 1877-79 (Fig. 4e), the only 3-year period on record with persistently low rainfall, and 1877 had the strongest rainfall deficits ($\sim$-2.0σ) within the 1870-2010 record. In the Eastern Cape and Natal regions in South Africa, October-March rainy season (Goddard and Graham 1999) rainfall was very high (>1σ) in 1874-75 and 1875-76 but very weak (<-1.2σ) in 1876-77 and 1877-78, with this 2-year average rainfall (1876-78) being the 5^{th} lowest between 1874-1995 (Fig. 4f).

Instrumental observations, tree ring-based measurements (Figs. 1-4), and historical documents all indicate that the most severe, persistent, and widespread impacts were in Asia (Davis 2001; Hao et al. 2010). We therefore quantify the spatial extent (fraction of area with PDSI<-1.0) and severity (area-average PDSI) of drought across Monsoon Asia (see inset in Fig. 5a for domain) within the ~800 year-long MADA record (1205-2012) from the MADA (Fig. 5). At its peak in 1877, the spatial extent of the drought was 48%, ranking a close second to the drought in 1495, which covered 49% of the domain (Fig. 5a). The 1877 drought was the most severe over the same period and by quite a large margin (Fig. 5b): area-weighted average PDSI for the Monsoon Asia region in 1877 was approximately -1.0, while no previous historical events exceeded -0.77. Although, the drought diminished in 1878 (area-average PDSI ~ -0.25), 32% of Monsoon Asia remained in drought (PDSI < -1.0). At least 25% of Monsoon Asia experienced droughts in all 3 years, with the 3-year average ranking 31^{st} highest in extent and 12^{th} in severity during this 800-year period.

Together, these multiple sources of data provide quantitative evidence of a severe, global-scale, multi-year drought between 1875-78 associated with record-setting droughts in several regions, particularly in Asia, where it was an extreme 3-year drought and the central year of 1877 was the worst single-year drought in the last 800 years.

3.2. Spatio-temporal characteristics of the drought in India

Within the regions impacted by the Great Drought, India is unique for its dense network of rain-gauge observations that extend back into the 19th century, and droughts in India have a close relationship with Pacific SST conditions. Using monthly, area-averaged, rain-gauge data across homogenous rainfall regions in India from the Indian Institute of Tropical Meteorology (IITM), we examine the characteristics of the drought in further detail. Figure 6 shows that the Great Drought started with dry conditions in peninsular India in winter 1875. Note that the winter monsoon typically brings ~30-60% of the annual rainfall to peninsular India (Rajeevan et al. 2012) (Fig. 6f). Following weak winter rainfall in late-1875, the All-India Rainfall (AIR) was anomalously low for most months (except July and September) in 1876 (Fig. 6a), particularly during the late monsoon and following early winter season. The winter season anomalies were particularly extreme in peninsular India, which experienced 4 consecutive months of near-record lows from Sep-Dec 1876, coinciding with the start of the famine in India (Fig. 6f). Intensifying the drought, multiple sub-regions including the Northwest, West Central and Central Northeast experienced consecutive near-record low rainfall during the 1877 monsoon months (Fig. 6b-e), consistent with the developing El Niño (Fig. 1) (Kumar et al. 2006; Pokhrel et al. 2012; Ihara et al. 2008). Though individual months have recorded lower rainfall in some sub-regions, the consistently low All-India Rainfall during the 1877 peak-monsoon season (Singh et al. 2014; Pai et al. 2016) is unsurpassed. Notably, 1876-77 is one of only two consecutive two-year periods with annual rainfall anomalies persistently lower than -1.0σ (-1.5σ in 1876 and -1.8σ in 1877), the other being 1904-05 though it had weaker anomalies. Rains over peninsular India recovered in the 1877 winter and were followed by very wet conditions in 1878 over all sub-regions except the Central Northeast (Fig. 6). These 1876-77 rainfall failures across many sub-regions of India, with its monsoon-dependent agriculture, contributed to the severe food shortage and ensuing famine in India that started in peninsular India in 1876. Subsequently, the extremely wet conditions in late-1877 and 1878 across India led to substantial loss of lives by facilitating the spread of infectious diseases in a famine-weakened population (Whitcombe 1993).

3.3. Natural Climate Variability: El Niño and Beyond

Pan-tropical rainfall failures, such as in 1877, are often caused by the warm phase of ENSO (Lyon and Barnston 2005). However, the precise impacts of an El Niño depends on its timing, duration, and location of peak SST anomalies (Kumar et al. 2006; Kumar 1999; Ihara et al. 2008). While previous studies of the 1876-78 pan-tropical drought attributed the blame to an El Niño (Aceituno et al. 2008; Hao et al. 2010; Kiladis and Diaz 1986), the reasons for the associated record severity of impacts in multiple regions have not yet been determined. Further, the other climate factors that contributed to the prolonged multi-year drought conditions before and after the El Niño are largely unexplored. Here, we examine the spatiotemporal features of the El Niño and identify the extraordinary sequence of SST configurations in three major ocean basins that led to this multi-year, global-scale extreme event (Fig. 1).

The 1877-78 El Niño was associated with the warmest annual-mean SSTs in the central Pacific (Niño 3.4 region) between 1870-2015 (Figs. 7a), consistent with the extreme impacts experienced across multiple regions and seasons (Fig. 1-3). The record high magnitude of the Niño3.4 anomalies in the instrumental record is consistent across multiple SST datasets (Fig. S2a). The annual-mean SLP at Darwin, Australia, another indicator of the strength of El Niños, suggests that the 1877 event was the 4th strongest between 1866-2015 (Fig. 7b). Although they differ in their estimates of the extremeness of the event due to the varying spatial signatures of different flavors of El Niños, both indicators suggest an extreme El Niño event. In addition to the extremely strong El Niño, we identify three other extreme or record-setting conditions that are responsible for the multi-year duration of this drought (Fig. 7). First, we find that anomalously cool tropical Pacific conditions preceded the El Niño and initiated droughts in some regions. Second, the North Atlantic was anomalously warm in 1877-79, with a peak following the peak of the El Niño (Fig. 7c). Third, a positive IOD event (Saji et al. 1999) developed in the latter half of 1877 along with the developing El Niño (Fig. 7d). These SST conditions that subsequently developed in the tropical Indian and Atlantic Oceans were extreme versions of their typical responses to El Niño (Alexander et al. 2002; Enfield and Mayer 1997; Elliott et al. 2001), and were crucial in shaping the overall multi-year drought in these different regions and seasons (Fig. 1).

During 1870-76, the central tropical Pacific was in a prolonged cool-phase for 7 years (Fig. 7a). This was associated with persistent and severe droughts in the western U.S. and much of Europe apart from the British Isles (Herweijer and Seager 2008) and persistently weak All-India winter rainfall (October-December) from 1871-1876 (Fig. 4b), consistent with the suppression of the winter monsoon during La Niña years (Rajeevan et al. 2012). The largest negative rainfall anomalies coincided with the strongest negative SST anomalies in 1875-76, and the start of the Great Drought in India in winter 1875. These low or negative SST anomalies (<0.2°C) persisted for ~80 consecutive months, the longest cool-period on record between 1870-present (Fig. 7a).

Coincident with the developing record El Niño was an unsurpassed positive IOD event in late-1877, with warm anomalies in the Somali Current region and cool SSTs off the western Australia coast (Fig. 7d, S2b-d). The DMI, a measure of this gradient across the Indian Ocean that typically peaks following the monsoon season, was the strongest on record (Fig. 7d). The very weak monsoon circulation associated with the extreme 1877 summer monsoon rainfall failure resulted in weak summertime cooling of the western Indian Ocean by upwelling and evaporation, which likely led to warmer SSTs in the region and the development of the positive IOD configuration. Positive IOD events that develop and peak during the monsoon season tend to enhance rainfall over the subcontinent but typical IOD events, such as the 1877 event that develop and peak in post-monsoon season (Sept-Nov), are normally associated with relatively weaker Indian Monsoon rainfall (Anil et al. 2016). To analyze the regional precipitation impacts of these individual and co-occurring conditions, we compare the composite July-December 20CR rainfall patterns during years (excluding 1877) with the following three conditions – (a) El Niño events without positive IOD events, (b) positive IOD events in the absence of El Niño events, and (c) co-occurring IOD and El Niño events (Fig. 8). The selected season coincides with the typical cycle of positive IOD events. We find that positive-IOD conditions amplify the drying effect of El Niños over parts of Southeast Asia, eastern Australia and southern Africa (Fig. 8a-c), consistent with previous studies (Ummenhofer et al. 2013; Goddard and Graham 1999; Cai et al. 2011, 2009; Ashok et al. 2003). All years when IOD events occurred along with developing El Niño events had severe rainfall deficits in these regions. While positive IOD conditions enhance rainfall over South Asia in the absence of El Niño events, rainfall is relatively suppressed when positive IOD events occur with an El Niño. Further, though central Asia does not show a robust rainfall response during either IOD or El Niño events, severe rainfall deficits occur across central Asia during all 5 years with co-occurring IOD and El Niño events (Fig. 8c). This suggests that the observed severity of rainfall deficits in these regions during 1877 is likely associated with the simultaneous occurrence of a record strong positive IOD and El Niño (Figs. 7). Basin-wide warming of the Indian Ocean followed in 1878 (Figs. 2c), which reduces the drying impacts of the continuing warm tropical Pacific SSTs on the 1878 India summer monsoon (Ihara et al. 2008).

Atlantic SSTs north of the Equator were anomalously warm in 1877, 1878 and 1879, shifting the Inter Tropical Convergence Zone (ITCZ) northward and causing three consecutive dry rainy seasons over the Nordeste region (Hastenrath and Greischar 1993; Uvo et al. 1998; Lucena et al. 2011) (Fig. 7c). The AMO Index, which represents SSTs in the North Atlantic (Schlesinger and Ramankutty 1994; Enfield et al. 2001), peaked three months after the peak of the El Niño to a record high magnitude between 1870-2015 (Fig. 1a). The severity of the impacts in the Brazilian Nordeste in 1878 are consistent with the warmest North Atlantic SSTs in that year (Fig. 7b). To evaluate the individual influence of these conditions on regional rainfall anomalies, we compare the composite February-May 20CR rainfall patterns during years (excluding 1877-78) with the following sets of conditions – (a) El Niño events during a neutral or cold phase of the AMO, (b) extreme positive AMO events in the absence of El Niños, and (c) El Niño events during a warm phase of the AMO (Fig. 8d-f). The February-May season coincides with the main rainy season in the Brazilian Nordeste and the peak warming in the North Atlantic following El Niños. El Niño events that occur in the cold or neutral AMO phase have a drying effect over northern Brazil though the impacts do not consistently extend into the Nordeste region (Fig. 8d). However, all 6 historical events with El Niño coinciding with warm AMO phases have more severe and widespread drying across northern and northeastern Brazil

(Fig. 8d-f), underscoring the importance of their combined occurrence in shaping the 1876-78 drought in this region.

3.4. Role of Tropical Pacific versus Global SST Forcing

To examine the relative role of the tropical Pacific including the 1877-78 El Niño relative to global SST anomalies unrelated to the tropical Pacific in driving regional precipitation anomalies, we compare precipitation anomalies from the 16-member GOGA and POGA-ML ensembles of climate simulations with the NCAR CCM3 (*see Section 2.5*). A comparison of these ensembles highlights the importance of SST anomalies outside of, and not forced by, the tropical Pacific that could aid in the predictability of future occurrences of a similar event.

For these comparisons, precipitation anomalies are calculated for the major rainy seasons in each region that experienced dry conditions – June-September summer and October-December winter monsoons in India, March-November in northeast China, October-March in South Africa and eastern Australia, January-March in the Mediterranean region and February-May in Nordeste Brazil (Fig. 9). Although the ensemble mean response does not simulate the rainfall deficits during the 1875 boreal winter monsoon in India (October-December), it does correctly simulate anomalously dry conditions in all other regions, albeit with lower magnitudes than observed in some regions. The simulated mean response of both ensembles shows a similar range of negative rainfall anomalies during 1877 boreal summer (July-September) monsoon season over India, 1877 boreal spring-fall (March-November) season in northeastern China, and 1877-78 austral spring-summer seasons (October-March) in Australia (Fig. 9) when these regions experienced the most severe dry conditions. In these regions, the distribution of precipitation anomalies from the two ensembles are indistinguishable at the 5% significance level, suggesting that the rainfall deficits during 1875-77 are largely forced by tropical Pacific SSTs or by SST anomalies in other regions that were forced by the tropical Pacific. This SST forcing includes the strong 1875-76 La Niña, the strong 1877-78 El Niño, and the 1877 positive IOD conditions. While the negative rainfall anomalies during October-December in India and March-November in East Asia are comparable, they are relatively smaller in magnitude to observations. Perhaps internal variability is driving the severity of these rainfall deficits but more likely, differences from observations are due to model deficiencies in accurately simulating the Asian monsoon rainfall and its teleconnections with natural modes of variability (Hurrell 1995), as discussed in *Section 2.5* (Fig. S1).

In contrast, negative rainfall anomalies during the 1877 and 1878 rainy seasons (February-May) over Nordeste Brazil (Fig. 9c-d), the 1877-78 austral summer season (October-March) in South Africa (Fig. 9g), and the 1878 winter rainy season (January-March) in the Mediterranean basin (Fig. 9h) cannot be attributed to the tropical Pacific forcing alone. For these regions, the GOGA and POGA-ML ensembles simulate significantly different distributions of rainfall anomalies with opposite or weaker mean rainfall responses in the latter. This suggests that these regional rainfall anomalies during 1877-78 are associated with SST variations outside the tropical Pacific that are unrelated to the El Niño, such as the North Atlantic extremely warm SSTs, or are not fully captured by the POGA-ML model, such as the late-1877 IOD even though that is likely a response to the El Niño. POGA-ML simulates near-zero average SST anomalies in the North Atlantic in spring 1877 though observed SST anomalies were positive (Fig. 9i). POGA-ML does simulate the warm North Atlantic response in 1878 to the strong El Niño, which occurs via atmospheric teleconnections and induced surface heat flux anomalies (Alexander et al. 2002; Enfield and Mayer 1997; Elliott et al. 2001) though the observed anomalies were significantly stronger (Fig. 9j). These differences in precipitation and SST anomalies suggest that the Brazil Nordeste rainfall deficits are intensified by the warm SST anomalies in the North Atlantic. Only in 1878 are these likely primarily a response to the El Niño. POGA-ML substantially underestimates the IOD response (Fig. 9k) because of the lack of ocean dynamics in the model configuration (Meyers et al. 2007). Consequently, greater and more robustly simulated precipitation drops over South Africa in 1877 in GOGA than POGA-ML could be attributed to the correct IOD state and magnitude in GOGA.

3.5. Comparison of the 1877-78 El Niño with other strong Niño events

We have shown that the occurrence of record warm North Atlantic and the strongest positive IOD event amplified the drying effects of El Niño events in several regions. Such conditions in the North Atlantic and Indian Oceans are not always linked to El Niño events (Meyers et al. 2007). The correlation between the Niño 3.4 and DMI indices is ~0.5 (p-value <<0.01) and between the Niño3.4 and AMO indices is ~0.35 (p-value <<0.01), which suggest that their co-variability is rare. A similar sequence of extreme conditions in these three basins has only occurred one other time in the instrumental record in 1997-1998. While the annual mean SST signal of the 1877-78 El Niño was comparable to the El Niños of 1997-98 (Fig. 7a), the impacts were far more severe in many regions in 1877-78. We identify four main differences in the spatio-temporal features of these events that explain the differing regional precipitation impacts between these events (Figs. 10-12).

First, the 1877-78 event was stronger and longer lasting than other notable El Niños, covering two summer monsoon seasons. SST anomalies exceeding 0.5°C in the Niño3.4 region lasted for 16 consecutive months during the 1876-78 period, 3 months longer than in 1997-98 and 2 months longer than in 1982-83 (Fig. 10a). The cumulative intensity of the 1877-78 event also exceeds all other El Niños between 1870-2013 (Fig. 10a). Second, although 1997-98 was the warmest of the three events in all Niño regions during the monsoon seasons, the largest warm anomalies were in the Niño1.2 region, the far eastern equatorial Pacific (Fig. 11a-d). While 1877-78 was less warm than the 1997-98 event in the central to eastern equatorial Pacific during the monsoon season, the region of peak anomalies in summer 1877 were west of those in 1997 (Fig. 11e). The location of the peak anomalies is relevant to understanding the regional impacts of the individual events. For instance, a stronger drought in South Asia in 1877 than in 1997 is consistent with previous modeling work showing a higher likelihood of westward-shifted than eastward-shifted El Niño events to produce subsidence and drought over the region (Kumar et al. 2006). Third, the 1997-98 El Niño developed rapidly in the eastern Pacific (Niño1.2 region) starting in February whereas the 1877 event development in this region started in June (Fig. 11a). This early and rapid development of the 1997-98 El Niño likely contributed to the early basin-wide warming of the Indian Ocean (Fig. 11e) that enhanced the moisture availability and weakened the suppression of convection typical of El Niño events. The IOD event during 1997 was weaker than during the 1877-78 El Niño event (Fig. 10b) and peaked later (Fig. 12a-b). Consequently, rainfall over India was near-normal in 1997 (Ihara et al. 2008) compared to the greater suppression of rainfall over India in 1877 that arose from the enhanced tropospheric stability associated with a warm tropical Pacific and a relatively cooler Indian Ocean (Ihara et al. 2008). Four, the North Atlantic warming following the 1997-98 event peaked in the following summer season rather than in the spring as in 1877-78 when it was able to suppress the main rainy season over northeastern Brazil (Fig. 12a-b). Further, the North Atlantic was warm in 1877 and 1878, which worked to weaken both rainy seasons in northeastern Brazil whereas the North Atlantic was relatively cooler in 1997 leading up to the 1997-98 El Niño event (Fig. 12a-b).

The 1877-78 event had substantially more severe and widespread drought conditions across Asia, northern Africa and parts of Europe than the 1997-98 event, and opposite hydroclimatic conditions over Australia (Fig. 12c-f). During the 1877 summer monsoon season, the westward-shifted peak SST anomalies in the Pacific led to peak positive moist static energy (MSE) anomalies and hence convection, occurring in the western-central Pacific, further west than both typical El Niño events and the 1997-98 event (Fig. 12g-h). Consequently, the surface high-pressure anomalies ($>2\sigma$) over the Indian continent were substantially larger during the summer monsoon in the developing phase of the 1877 El Niño than during 1997 (Fig. 12i-j), leading to a greater weakening of the MSE ($<-1.5\sigma$) over the peak region of the Indian monsoon circulation (Boos and Kuang 2010; Cane 2010). Combined with its enormous magnitude, this particular SST anomaly pattern in 1877 was also associated with anomalously high surface pressure ($>2\sigma$) across much of central, northern and eastern Asia, and the Maritime Continent, during the summer monsoon season, substantially larger and more widespread than in 1997 (Fig. 12i-j). Accordingly, these regions experienced stronger suppression of MSE ($<-1.5\sigma$) and more extreme precipitation deficits in 1877 than in 1997. The exception is Indonesia which had stronger drought conditions in 1997. In eastern Australia, drought was severe and widespread in 1877-78 but largely concentrated in southeastern Australia in 1997-98 with wetter conditions across the rest of the region. These differences were associated with the stronger positive IOD event in 1877 and the substantially cooler temperatures off the northern and western coast of Australia, which lead to greater suppression of moisture availability, MSE, and precipitation across a large part of eastern Australia (Fig. 12c-d,g-f).

4. Discussion and Conclusions

Our analysis leads to three main findings. First, multiple sources of data reveal an intense, global-scale drought affecting many tropical and subtropical regions simultaneously between 1876-78, with record-setting conditions in Asia where there were the highest number of reported famine victims (Davis 2001). While single-year droughts might not have severe societal impacts, these severe and prolonged climatic conditions undoubtedly initiated the Global Famine crisis. Second, this event was associated with the strongest El Niño event in the instrumental record, which followed the longest cool-period in the tropical Pacific, and whose early evolution, long duration, and cumulative intensity relative to other strong El Niños, accounts for the severity of its global impacts. The magnitude of the 1877-78 El Niño SST anomalies were likely more extreme than in the reconstructed datasets: the paucity of SST observations in the tropical Pacific in the late 19th century can only lead to underestimating its strength (Kaplan et al. 1998). Third, this multi-year, global-scale extreme event was largely orchestrated by the tropical Pacific via direct atmospheric teleconnections and then indirectly by influencing pan-tropical SSTs that additionally drove the regional droughts. Record warm conditions in the North Atlantic in 1878 and the record positive IOD conditions in 1877 resulting from the cascading influence of this powerful El Niño were critical in shaping its regional impacts, particularly on Nordeste Brazil, northern and southern Africa, and eastern Australia, during and after the 1877 El Niño. However, the independently warm North Atlantic in 1877 aided the development of drought in Nordeste Brazil, prior to the evolution of the El Niño.

While data coverage in 1877 was spare in the Pacific Basin, with availability only at a few points in the Central Pacific, the extreme magnitude of this event, corroborated by multiple reconstructed SST datasets (Fig. S2), has little uncertainty. Extensive tests conducted by Kaplan et al. (Kaplan et al. 1998), where the input data coverage for the reconstructed SST product was withheld to the coverage in the 1870s, shows that this change in coverage does not substantially influence the magnitude of reconstructed SSTs in the tropical Pacific, particularly during notable El Niño events. The Indian and Atlantic Oceans had much greater data coverage than the Pacific and consequently lower errors and uncertainties for this time period.

Exacerbated by prevailing social conditions, famines followed the occurrence of severe droughts across the world (Davis 2001). In India, despite agricultural losses associated with the drought, British colonialists collected harsh taxes, hoarded and exported grain from India to England, and destroyed common resources that traditionally buffered societies from climate variability (Davis 2001; Meena 2015). Food shortage beginning in 1875, depleted local reserves and high prices made food inaccessible to the starving local population, who were ultimately denied labor for being weak (Davis 2001). In northern China, disruption of the agrarian societies by imperialist forces and a dysfunctional transportation system that made relief hard to access, led to widespread death and depopulation of vast communities starting in 1877, following a year of drought (Davis 2001). In the Brazilian Nordeste, the Great Drought devastated the cotton and cattle raising important to the regional economy and subsistence farmers alike. Initially, the people of the Sertão remained but with starvation spreading and the drought persisting out-migration followed creating social instability across a wider region (Greenfield 1992; Davis 2001). As in India, the official response was to create work camps and exchange aid for labor. Smallpox broke out in the camps greatly increasing the mortality (Davis 2001). By the end of the Great Drought in 1880 up to one million were dead and it is claimed the Nordeste never fully recovered (Cuniff 1970). In Algeria and Morocco, the drought and failed crops forced peasants to sell their wealth, cattle and sheep, for export to France, further impoverishing the population. As in India and the Nordeste, out-migration soon followed with concentrations of migrants leading to cholera and typhoid and increased mortality (Davis 2001).

The Great Drought and the Global Famine cast a long shadow on politics and economy across the tropics. The demographic disruption cast by the famines often lasted for generations: in the Chinese province of Shanxi, for example, it took until 1953 to regain the 1875 population levels (Davis 2001). The decimation of agricultural workforces, along with the destruction of local means of production (in northern China starving peasants actually ate their homes, constructed of sorghum stalks), prostrated traditional Asian and African societies in the face of the colonizing wave of the late 19th Century. Starvation amongst the African population facilitated the French colonial expansion in North Africa and the eventual British defeat of the famine-weakened Zulu Nation in summer 1879 ((Davis 2001) and references therein). In a very real sense, the El Niño and climate events of 1876-78 helped create the global inequalities that would later be characterized as ‘first’ and ‘third worlds’.

The severe and widespread 1876-78 drought in multiple grain-producing regions of the world was induced by natural SST variability. Therefore, such a global-scale event might happen again. With the projected intensification of El Niño-induced hydroclimate anomalies due to rising greenhouse gas concentrations and global warming (Seager et al. 2012; Cai et al. 2014), such widespread droughts could become even more severe. While the socio-political factors that translated the Great Drought into unprecedented famine (Davis 2001) do not exist in the current world, such extreme events would still lead to severe shocks to the global food system with local food insecurity in vulnerable countries potentially amplified by today's highly connected global food trade network (Puma et al. 2015). Continued improvements in understanding why this event, and the coupled atmosphere-ocean processes it induced across the tropics, led to such a devastating global drought should translate into improved prediction of the consequences of any such future event and allow effective management of the resulting food crises, so that the next Great Drought does not trigger another Great Famine.

Acknowledgments

General: We would like to thank the National Oceanic and Atmospheric Administration (NOAA) and the Indian Institute of Tropical Meteorology (IITM) for archiving and enabling public access to their data. ERSSTv4 data, Twentieth Century Reanalysis version 2c, and time series of all indices, were provided by NOAA ESRL PSD, Boulder, Colorado. GHCN data was provided by NOAA's National Centers for Environmental Information (NCEI). Support for the NOAA-CIRES Twentieth Century Reanalysis Project version 2c dataset is provided by the U.S. Department of Energy, Office of Science Biological and Environmental Research (BER), and by the National Oceanic and Atmospheric Administration Climate Program Office. The rainfall time series for India, which are derived from the original rainfall records maintained by the Indian Meteorological Department, were provided by IITM. We acknowledge NCEI for maintaining the World Data Center for Paleoclimatology archives. We also thank Alexey Kaplan for assistance with the Dipole Mode Index data and Hun Baek for valuable discussions on the AMO.

Funding: D. Singh was supported by the Lamont-Doherty Earth Observatory Fellowship. R. Seager and M.A. Cane were supported by NSF OCE1657209. B.I. Cook was supported by the NASA Modeling, Analysis, and Prediction program. M. Ting was supported by NOAA grant

NA14OAR4310223 and NSF grant AGS 16-07348. We acknowledge the support of the World Surf League P.U.R.E. and the Center for Climate and Life at Lamont-Doherty Earth Observatory.

Author contributions: DS designed the analysis, analyzed the data, performed the research, and wrote the paper. RS, MC, BIC and MT contributed to the design of the study. All authors contributed to the interpretation of results and writing of the manuscript.

Competing interests: The authors declare no competing interests.

Data and materials availability: All data used in the analysis are from publicly available datasets for which sources have been provided in the Materials and Methods section.

References

Aceituno, P., R. Prieto, M. Eugenia, S. Alejandra, G. Poveda, and M. Falvey, 2008: The 1877 – 1878 El Niño episode : associated impacts in South America. *Clim. Change*, 389–416, doi:10.1007/s10584-008-9470-5.

Alexander, M. A., I. Bladé, M. Newman, J. R. Lanzante, N.-C. Lau, and J. D. Scott, 2002: The Atmospheric Bridge: The Influence of ENSO Teleconnections on Air–Sea Interaction over the Global Oceans. *J. Clim.*, **15**, 2205–2231, doi:10.1175/1520-0442(2002)015<2205:TABTIO>2.0.CO;2.

Allan, R. J., C. J. C. Reason, P. Carroll, and P. D. Jones, 2002: A reconstruction of Madras (Chennai) mean sea-level pressure using instrumental records from the late 18th and early 19th centuries. *Int. J. Climatol.*, **22**, 1119–1142, doi:10.1002/joc.678.

Anil, N., M. R. Ramesh Kumar, R. Sajeev, and P. K. Saji, 2016: Role of distinct flavours of IOD events on Indian summer monsoon. *Nat. Hazards*, **82**, 1317–1326, doi:10.1007/s11069-016-

2245-9.
Ashok, K., Z. Guan, and T. Yamagata, 2003: Influence of the Indian Ocean Dipole on the Australian winter rainfall. *Geophys. Res. Lett.*, **30**, n/a-n/a, doi:10.1029/2003GL017926.
Baek, S. H., J. E. Smerdon, S. Coats, A. P. Williams, B. I. Cook, E. R. Cook, and R. Seager, 2017: Precipitation, temperature, and teleconnection signals across the combined North American, Monsoon Asia, and Old World Drought Atlases. *J. Clim.*, in press.
Barnston, A. G., M. Chelliah, and S. B. Goldenberg, 1997: Documentation of a highly ENSO-related sst region in the equatorial pacific: Research note. *Atmosphere-Ocean*, **35**, 367–383, doi:10.1080/07055900.1997.9649597. http://dx.doi.org/10.1080/07055900.1997.9649597.
Blanford, H. F., 1887: The Eleven-Year Periodical Fluctuation of the Carnatic Rainfall. *Nature*, **36**, 227.
Boos, W. R., and Z. Kuang, 2010: Dominant control of the South Asian monsoon by orographic insulation versus plateau heating. *Nature*, **463**, 218–222.
Buchan, A., 1877: Meteorology and the Indian Famine. *Nature*, **16**, 425.
Cai, W., T. Cowan, and M. Raupach, 2009: Positive Indian Ocean Dipole events precondition southeast Australia bushfires. *Geophys. Res. Lett.*, **36**, n/a-n/a, doi:10.1029/2009GL039902. http://dx.doi.org/10.1029/2009GL039902.
Cai, W., P. van Rensch, T. Cowan, and H. H. Hendon, 2011: Teleconnection Pathways of ENSO and the IOD and the Mechanisms for Impacts on Australian Rainfall. *J. Clim.*, **24**, 3910–3923, doi:10.1175/2011JCLI4129.1. https://doi.org/10.1175/2011JCLI4129.1.
——, and Coauthors, 2014: Increasing frequency of extreme El Nino events due to greenhouse warming. *Nat. Clim. Chang.*, **4**, 111–116.

Cane, M. A., 2010: Climate: A moist model monsoon. *Nature*, **463**, 163–164.

Clarke, H., 1878: The Drought. *Nature*, **19**, 53.

Cook, E. R., 2015: Asian monsoon variability over the past millennium reconstructed from long tree-ring records: the Monsoon Asia Drought Atlas, version 2 (MADAv2). *Asian monsoon variability over the past millennium reconstructed from long tree-ring records: the Monsoon Asia Drought Atlas, version 2 (MADAv2). Presented at the AGU Chapman Conference: "Evolution of the Asian Monsoon and its Impact on Landscape, Environ*, Hong Kong SAR, China, June 14-18.

Cook, E. R., R. Seager, M. A. Cane, and D. W. Stahle, 2007: North American drought: Reconstructions, causes, and consequences. *Earth-Science Rev.*, **81**, 93–134, doi:10.1016/j.earscirev.2006.12.002. http://linkinghub.elsevier.com/retrieve/pii/S0012825206001784.

Cook, E. R., K. J. Anchukaitis, B. M. Buckley, R. D. D'Arrigo, G. C. Jacoby, and W. E. Wright, 2010a: Asian Monsoon Failure and Megadrought During the Last Millennium. *Science,* **328**, 486–489, doi:10.1126/science.1185188. http://www.sciencemag.org/cgi/doi/10.1126/science.1185188.

——, R. Seager, R. R. Heim, R. S. Vose, C. Herweijer, and C. Woodhouse, 2010b: Megadroughts in North America: placing IPCC projections of hydroclimatic change in a long-term palaeoclimate context. *J. Quat. Sci.*, **25**, 48–61, doi:10.1002/jqs.1303. http://dx.doi.org/10.1002/jqs.1303.

——, and Coauthors, 2015: Old World megadroughts and pluvials during the Common Era. *Sci. Adv.*, **1**.

Cuniff, R. L., 1970: The Great Drought: Northeast Brazil, 1877–1880. .

Davis, M., 2001: *Late Victorian Holocausts: El Nino Famines and the Making of the Third World*. Verso, New York, NY,.

Derby, O. A., 1878: The Rainfall of Brazil and the Sun-Spots. *Nature*, **18**, 384.

Elliott, J. R., S. P. Jewson, and R. T. Sutton, 2001: The Impact of the 1997/98 El Niño Event on the Atlantic Ocean. *J. Clim.*, **14**, 1069–1077, doi:10.1175/1520-0442(2001)014<1069:TIOTEN>2.0.CO;2. https://doi.org/10.1175/1520-0442(2001)014%3C1069:TIOTEN%3E2.0.CO.

Enfield, D. B., and D. A. Mayer, 1997: Tropical Atlantic sea surface temperature variability and its relation to El Niño-Southern Oscillation. *J. Geophys. Res. Ocean.*, **102**, 929–945, doi:10.1029/96JC03296. http://dx.doi.org/10.1029/96JC03296.

——, A. M. Mestas-Nuñez, and P. J. Trimble, 2001: The Atlantic Multidecadal Oscillation and its relation to rainfall and river flows in the continental U.S. *Geophys. Res. Lett.*, **28**, 2077–2080, doi:10.1029/2000GL012745. http://dx.doi.org/10.1029/2000GL012745.

Goddard, L., and N. E. Graham, 1999: Importance of the Indian Ocean for simulating rainfall anomalies over eastern and southern Africa. *J. Geophys. Res. Atmos.*, **104**, 19099–19116, doi:10.1029/1999JD900326. http://dx.doi.org/10.1029/1999JD900326.

Gráda, C. O., 2009: *Famine: A short Story*. Princeton University Press,.

Greenfield, G. M., 1992: The Great Drought and Elite Discourse in Imperial Brazil. *Hisp. Am. Hist. Rev.*, **72**, 375–400, doi:10.2307/2515990. http://www.jstor.org/stable/2515990.

Hao, Z., J. Zheng, G. Wu, X. Zhang, and Q. Ge, 2010: 1876–1878 severe drought in North China: Facts, impacts and climatic background. *Chinese Sci. Bull.*, **55**, 3001–3007, doi:10.1007/s11434-010-3243-z. http://link.springer.com/10.1007/s11434-010-3243-z.

Harris, I., P. D. Jones, T. J. Osborn, and D. H. Lister, 2014: Updated high-resolution grids of monthly climatic observations - the CRU TS3.10 Dataset. *Int. J. Climatol.*, **34**, 623–642, doi:10.1002/joc.3711.

Hasell, J., and M. Roser, 2017: Famines. *Our World Data*,. https://ourworldindata.org/famines.

Hastenrath, S., and L. Greischar, 1993: Circulation mechanisms related to northeast Brazil rainfall anomalies. *J. Geophys. Res. Atmos.*, **98**, 5093–5102, doi:10.1029/92JD02646. http://doi.wiley.com/10.1029/92JD02646.

Herweijer, C., and R. Seager, 2008: The global footprint of persistent extra-tropical drought in the instrumental era. *Int. J. Climatol.*, **28**, 1761–1774, doi:10.1002/joc.1590. http://dx.doi.org/10.1002/joc.1590.

Huang, B., and Coauthors, 2014: Extended Reconstructed Sea Surface Temperature Version 4 (ERSST.v4). Part I: Upgrades and Intercomparisons. *J. Clim.*, **28**, 911–930, doi:10.1175/JCLI-D-14-00006.1. https://doi.org/10.1175/JCLI-D-14-00006.1.

Hunter, W. W., 1877: The Cycle of Droughts and Famines in Southern India. *Nature*, **16**, 14.

Hurrell, J. W., 1995: Comparison of NCAR community climate model (CCM) climates. *Clim. Dyn.*, **11**, 25–50, doi:10.1007/BF00220675. https://doi.org/10.1007/BF00220675.

Ihara, C., Y. Kushnir, M. A. Cane, and A. Kaplan, 2008: Timing of El Niño–Related Warming and Indian Summer Monsoon Rainfall. *J. Clim.*, **21**, 2711–2719, doi:10.1175/2007JCLI1979.1. http://journals.ametsoc.org/doi/abs/10.1175/2007JCLI1979.1.

JISAO, Joint Institute for the Study of Atmosphere and Oceans, University of Washington Datasets. http://research.jisao.washington.edu/data_sets/brazil/fortaleza.

Kang, S., B. Yang, C. Qin, J. Wang, F. Shi, and J. Liu, 2013: Extreme drought events in the years 1877–1878, and 1928, in the southeast Qilian Mountains and the air–sea coupling system. *Quat. Int.*, **283**, 85–92, doi:http://dx.doi.org/10.1016/j.quaint.2012.03.011. http://www.sciencedirect.com/science/article/pii/S1040618212001577.

Kaplan, A., M. A. Cane, Y. Kushnir, A. C. Clement, M. B. Blumenthal, and B. Rajagopalan, 1998: Analyses of global sea surface temperature 1856–1991. *J. Geophys. Res. Ocean.*, **103**, 18567–18589, doi:10.1029/97JC01736. http://dx.doi.org/10.1029/97JC01736.

Kiladis, G. N., and H. F. Diaz, 1986: An Analysis of the 1877–78 ENSO Episode and Comparison with 1982–83. *Mon. Weather Rev.*, **114**, 1035–1047, doi:10.1175/1520-0493(1986)114<1035:AAOTEE>2.0.CO;2. https://doi.org/10.1175/1520-0493(1986)114%3C1035:AAOTEE%3E2.0.CO.

Kumar, K. K., 1999: On the Weakening Relationship Between the Indian Monsoon and ENSO. *Science*, **284**, 2156–2159, doi:10.1126/science.284.5423.2156. http://www.sciencemag.org/content/284/5423/2156.abstract.

——, B. Rajagopalan, M. Hoerling, G. Bates, and M. Cane, 2006: Unraveling the Mystery of Indian Monsoon Failure During El Niño. *Science*, **314**, 115–119, doi:10.1126/science.1131152.

Lawrimore, J. H., M. J. Menne, B. E. Gleason, C. N. Williams, D. B. Wuertz, R. S. Vose, and J. Rennie, 2011: An overview of the Global Historical Climatology Network monthly mean temperature data set, version 3. *J. Geophys. Res.J*, **116**, doi:10.1029/2011JD016187.

Lee, D. E., and M. Biasutti, 2014: Climatology and Variability of Precipitation in the Twentieth-Century Reanalysis. *J. Clim.*, **27**, 5964–5981, doi:10.1175/JCLI-D-13-00630.1. https://doi.org/10.1175/JCLI-D-13-00630.1.

Lucena, D. B., J. Servain, and M. F. Gomes Filho, 2011: Rainfall Response in Northeast Brazil from Ocean Climate Variability during the Second Half of the Twentieth Century. *J. Clim.*,

24, 6174–6184, doi:10.1175/2011JCLI4194.1. https://doi.org/10.1175/2011JCLI4194.1.

Lyon, B., and A. G. Barnston, 2005: ENSO and the Spatial Extent of Interannual Precipitation Extremes in Tropical Land Areas. *J. Clim.*, **18**, 5095–5109, doi:10.1175/JCLI3598.1.

Meena, H. K., 2015: Famine in Late 19th Century India : Natural or Man-Made. *J. Hum. Soc. Sci. Res.*, **06**, 35–44.

Meyers, G., P. McIntosh, L. Pigot, and M. Pook, 2007: The Years of El Niño, La Niña, and Interactions with the Tropical Indian Ocean. *J. Clim.*, **20**, 2872–2880, doi:10.1175/JCLI4152.1. https://doi.org/10.1175/JCLI4152.1.

Pai, D. S., L. Sridhar, and M. R. Ramesh Kumar, 2016: Active and break events of Indian summer monsoon during 1901--2014. *Clim. Dyn.*, **46**, 3921–3939, doi:10.1007/s00382-015-2813-9.

Palmer, J. G., and Coauthors, 2015: Drought variability in the eastern Australia and New Zealand summer drought atlas (ANZDA, CE 1500–2012) modulated by the Interdecadal Pacific Oscillation. *Environ. Res. Lett.*, **10**, 124002.

Parthasarathy, B., N. A. Sontakke, A. A. Monot, and D. R. Kothawale, 1987: Droughts/floods in the summer monsoon season over different meteorological subdivisions of India for the period 1871–1984. *J. Climatol.*, **7**, 57–70, doi:10.1002/joc.3370070106. http://dx.doi.org/10.1002/joc.3370070106.

——, K. R. Kumar, and A. A. Munot, 1993: Homogeneous Indian Monsoon rainfall: Variability and prediction. *Proc. Indian Acad. Sci. - Earth Planet. Sci.*, **102**, 121–155, doi:10.1007/BF02839187. https://doi.org/10.1007/BF02839187.

——, A. A. Munot, and D. R. Kothawale, 1994: All-India monthly and seasonal rainfall series: 1871--1993. *Theor. Appl. Climatol.*, **49**, 217–224, doi:10.1007/BF00867461.

https://doi.org/10.1007/BF00867461.

——, ——, and ——, 1995: *Monthly and seasonal rainfall series for all-India homogeneous regions and meteorological subdivisions : 1871-1994. Research Report No. RR-065*. Pune, India, 113 pp.

Pokhrel, S., H. S. Chaudhari, S. K. Saha, A. Dhakate, R. K. Yadav, K. Salunke, S. Mahapatra, and S. A. Rao, 2012: ENSO, IOD and Indian Summer Monsoon in NCEP climate forecast system. *Clim. Dyn.*, **39**, 2143–2165, doi:10.1007/s00382-012-1349-5.

Polzin, D., and S. Hastenrath, 2014: CLIMATE OF BRAZIL ’ S NORDESTE AND TROPICAL ATLANTIC SECTOR : PREFERRED TIME SCALES OF VARIABILITY DIERK POLZIN , STEFAN HASTENRATH University of Wisconsin-Madison , Atmospheric and Oceanic Sciences , Madison , Wisconsin , USA Received September 2013 - Ac. *Rev. Bras. Meteorol.*, **29**, 153–160.

Puma, M. J., S. Bose, S. Y. Chon, and B. I. Cook, 2015: Assessing the evolving fragility of the global food system. *Environ. Res. Lett.*, **10**, 24007.

Rajeevan, M., C. K. Unnikrishnan, J. Bhate, K. Niranjan Kumar, and P. P. Sreekala, 2012: Northeast monsoon over India: Variability and prediction. *Meteorol. Appl.*, **19**, 226–236, doi:10.1002/met.1322. http://dx.doi.org/10.1002/met.1322.

Rayner, N. A., D. E. Parker, E. B. Horton, C. K. Folland, L. V Alexander, D. P. Rowell, E. C. Kent, and A. Kaplan, 2003: Global analyses of sea surface temperature, sea ice, and night marine air temperature since the late nineteenth century. *J. Geophys. Res. Atmos.*, **108**, n/a-n/a, doi:10.1029/2002JD002670. http://dx.doi.org/10.1029/2002JD002670.

Reynolds, R. W., and T. M. Smith, 1994: Improved Global Sea Surface Temperature Analyses Using Optimum Interpolation. *J. Clim.*, **7**, 929–948, doi:10.1175/1520-

0442(1994)007<0929:IGSSTA>2.0.CO;2. https://doi.org/10.1175/1520-0442(1994)007%3C0929:IGSSTA%3E2.0.CO.

Ropelewski, C. F., and M. S. Halpert, 1987: Global and Regional Scale Precipitation Patterns Associated with the El Niño/Southern Oscillation. *Mon. Weather Rev.*, **115**, 1606–1626, doi:10.1175/1520-0493(1987)115<1606:GARSPP>2.0.CO;2. https://doi.org/10.1175/1520-0493(1987)115%3C1606:GARSPP%3E2.0.CO.

Saji, N. H., 2003: Possible impacts of Indian Ocean Dipole mode events on global climate . *Clim. Res.*, **25**, 151–169. http://www.int-res.com/abstracts/cr/v25/n2/p151-169/.

——, B. N. Goswami, P. N. Vinayachandran, and T. Yamagata, 1999: A dipole mode in the tropical Indian Ocean. *Nature*, **401**, 360. http://dx.doi.org/10.1038/43854.

Schlesinger, M. E., and N. Ramankutty, 1994: An oscillation in the global climate system of period 65-70 years. *Nature*, **367**, 723–726. http://dx.doi.org/10.1038/367723a0.

Seager, R., Y. Kushnir, C. Herweijer, N. Naik, and J. Velez, 2005: Modeling of Tropical Forcing of Persistent Droughts and Pluvials over Western North America: 1856–2000. *J. Clim.*, **18**, 4065–4088, doi:10.1175/JCLI3522.1. https://doi.org/10.1175/JCLI3522.1.

——, N. Naik, and L. Vogel, 2012: Does Global Warming Cause Intensified Interannual Hydroclimate Variability?*. *J. Clim.*, **25**, 3355–3372, doi:10.1175/JCLI-D-11-00363.1. http://journals.ametsoc.org/doi/abs/10.1175/JCLI-D-11-00363.1.

Singh, D., M. Tsiang, B. Rajaratnam, N. S. Diffenbaugh, and N. S. Di, 2014: Observed changes in extreme wet and dry spells during the South Asian summer monsoon season. *Nat. Clim. Chang.*, **4**, 1–6, doi:10.1038/NCLIMATE2208.

Slingo, J. M., and H. Annamalai, 2000: 1997: The El Niño of the Century and the Response of the Indian Summer Monsoon. *Mon. Weather Rev.*, **128**, 1778–1797, doi:10.1175/1520-

0493(2000)128<1778:TENOOT>2.0.CO;2. http://dx.doi.org/10.1175/1520-0493(2000)128%3C1778:TENOOT%3E2.0.CO;2.

Trenberth, K., 1984: SOI Data provided by the Climate Analysis Section. Update Regularly.

Trenberth, K., and NCAR Staff, 2016: The Climate Data Guide: Southern Oscillation Indices: Signal, Noise and Tahiti/Darwin SLP (SOI). https://climatedataguide.ucar.edu/climate-data/southern-oscillation-indices-signal-noise-and-tahitidarwin-slp-soi (Accessed March 2, 2016).

Trenberth, K. E., and D. P. Stepaniak, 2001: Indices of El Niño Evolution. *J. Clim.*, **14**, 1697–1701, doi:10.1175/1520-0442(2001)014<1697:LIOENO>2.0.CO;2. https://doi.org/10.1175/1520-0442(2001)014%3C1697:LIOENO%3E2.0.CO.

Ummenhofer, C. C., R. D. D. Arrigo, and E. R. Cook, 2013: Links between Indo-Pacific climate variability and drought in the Monsoon Asia Drought Atlas. *Cimate Dyn.*, **40**, 1319–1334, doi:10.1007/s00382-012-1458-1.

Uvo, C. B., C. A. Repelli, S. E. Zebiak, and Y. Kushnir, 1998: The Relationships between Tropical Pacific and Atlantic SST and Northeast Brazil Monthly Precipitation. *J. Clim.*, **11**, 551–562, doi:10.1175/1520-0442(1998)011<0551:TRBTPA>2.0.CO;2. https://doi.org/10.1175/1520-0442(1998)011%3C0551:TRBTPA%3E2.0.CO.

Wang, B., J. Li, and Q. He, 2017: Variable and robust East Asian monsoon rainfall response to El Niño over the past 60 years (1957–2016). *Adv. Atmos. Sci.*, **34**, 1235–1248, doi:10.1007/s00376-017-7016-3.

Whitcombe, E., 1993: Famine Mortality. *Econ. Polit. Wkly.*, **28**, 1169–1173.

Xu, Z. X., K. Takeuchi, and H. Ishidaira, 2004: Correlation between El Niño–Southern Oscillation (ENSO) and precipitation in South-east Asia and the Pacific region. *Hydrol.*

Process., **18**, 107–123, doi:10.1002/hyp.1315. http://dx.doi.org/10.1002/hyp.1315.

Figures and Tables

Figure 1. Drought extent and SST evolution: (a) Monthly evolution of the Niño3.4 Index, Atlantic Multidecadal Oscillation (AMO) Index, and the Indian Ocean Dipole Mode Index (DMI) during the Global Famine of 1876-1878. The approximate beginning and duration of dry conditions in major regions based on PDSI values (<-1.0) or seasonal rainfall anomalies ($<-1.0\sigma$), or a combination of both, are indicated by arrows and lines. Since PDSI from the regional drought atlases is annually resolved, the duration of drought in the regions identified based on PDSI (i.e East Asia, North Africa, and SE Asia) are indicated for the 12-month period ending in the reconstruction season (i.e Sep-Aug for MADA, OWDA, and NADA). Grey lines indicate seasons outside the main rainy seasons. (b) Extent of dry conditions (colored regions) during each of the three years based on negative PDSI (<-1.0; brown) or low rainfall ($<-1.0\sigma$; pink) conditions. Grey areas highlight the extent of the drought atlases and white areas indicate absence of data. To identify the characteristics of dry conditions, PDSI values are from the regional drought atlases and rainfall anomalies (relative to 1901-1950) are from the GHCN database. Note: the dry regions depicted in panels (b) are approximate and for illustrative purposes. Some sub-regions within the broader area depicted here might have differing conditions.

Figure 2. The Great Drought 1876-78: Sep-Aug (12-month) average sea-surface temperature (SST) anomalies during 1875-76, 1876-77 and 1877-78; and Palmer Drought Severity Index (PDSI) from the drought atlases for each of the three years. MADA, NADA, and OWDA provide June-August PDSI and ANZDA provides the December-February PDSI. Since PDSI integrates the moisture supply and demand over preceding seasons, we provide average detrended SST anomalies for the 12-month period from the preceding September to the concurrent August. SST anomalies are calculated relative to the 1901-1950 baseline period.

Figure 3. Global rainfall anomalies during the Great Drought: Standardized anomalies of 12-month (Sep-Aug) cumulative rainfall at available GHCN stations during the three periods: (a) 1875-76, (b) 1876-77, and (c) 1877-78. Anomalies are with reference to the 1901-1950 climatology.

Figure 4. Severity of Rainfall Anomalies: Time series of (a) standardized anomalies of summer (Jun-Sep) monsoon rainfall for the All India region, (b) standardized anomalies of winter (Oct-Dec) monsoon rainfall for the All India region, (c) sea-level pressure at Madras, India, (d) standardized anomalies of Mar-Nov rainfall at Shanghai, China, (e) standardized anomalies of Feb-May rainfall at Fortaleza in the Brazil Nordeste, and (f) standardized anomalies of Oct-Mar rainfall in eastern South Africa (average of 6 stations in the Eastern Cape and KwaZulu-Natal provinces). The 4 red dots highlight years from 1875 to 1878, and the horizontal red line indicates the magnitude of the peak anomalies within this 4-year period for reference. The length of the Madras SLP record is limited by the length of the available timeseries and the South African rainfall timeseries is limited by the unavailability of data at multiple stations in the GHCN database post-1997. Rainfall for the 1997-1998 rainy seasons at Fortaleza are missing in the record. Gaps in any of the records represent missing values. Anomalies are calculated from the 1901-1950 baseline period**.**

Figure 5. Monsoon Asia Drought Severity and Extent: Time series of (a) the fraction of the Monsoon Asia region (inset) experiencing drought (PDSI <-1.0), expressed as a percent, and (b) the area-weighted average PDSI across the region from 1205-2012. The drought severity and extent for each year of the drought is indicated in the corresponding panels. Dashed grey lines indicate the magnitude of these characteristics during the peak of the drought in 1877. The 1877 drought extent is the second highest and drought severity is the strongest since the early 1200s.

Figure 6. Temporal evolution of drought over India: Rainfall for the All India domain and 5 sub-regions defined by the Indian Institute of Tropical Meteorology (IITM) based on the similarity in their rainfall characteristics (refer Fig. 2 in Parthasarathy et al. (1995) or http://www.tropmet.res.in/IITM/region-maps.html). Colored lines highlight the evolution of drought across different regions between 1875 and 1878. Grey colors show all other years between 1870-2013.

Figure 7. ENSO and SST features: Long-term de-trended time-series of the (a) Niño 3.4 Index, (b) Darwin sea-level pressure anomalies (hPa), (c) AMO Index, and (d) Indian Ocean Dipole Mode Index (DMI). Dashed red lines indicate the peak magnitude of the index between 1876-78. Vertical blue lines in panel (a) highlight the 4 longest prolonged cool periods in the equatorial Pacific, which are defined as consecutive months with Niño3.4 SST anomalies consistently below 0.2˚C. Anomalies are calculated from the 1901-1950 baseline period.

Figure 8. Influence of different ocean basins: Composite standardized rainfall anomalies for Jul-Dec from 20CR during (a) years with developing El Nino events without positive IOD events, (b) years with positive IOD events without concurrent El Nino events, and (c) years with positive IOD and developing El Nino events. Jul-Dec is selected to coincide with the cycle of positive IOD events. Composite average rainfall anomalies for Feb-May during (d) years with strong El Nino events during non-positive (neutral or negative) AMO events, (e) years with positive AMO events without El Nino events, and (f) years with strong El Nino events during positive AMO phases. Feb-May is selected to coincide with the peak rainy season over Nordeste Brazil and the peak AMO following a strong El Nino event. El Nino events are selected based on Nov-Mar Nino 3.4 index exceeding 1.0σ. (Note that years in the left column indicate years of developing El Nino events.). Positive AMO events are selected based on Feb-May AMO index exceeding 1.0σ. Positive IOD events are selected based on July-Dec DMI Index >1.0σ. Standardized rainfall anomalies are calculated based on the mean and standard deviation (σ) of the baseline period 1901-1950.

Figure 9. Role of Tropical Pacific versus Global Oceans: (a-h) Standardized rainfall anomalies in years associated with extreme deficits in different regions (see red boxes on map) from the 16-member ensemble of (black) GOGA and (red) POGA-ML simulations. For each region, seasons are chosen to coincide with the local main rainy seasons. Observed average rainfall anomalies for each region are indicated by blue diamonds. Average Feb-May North Atlantic (0-70°N, 80°W-0) surface temperature (TS) anomalies in (i) 1877 and (j) 1878, and average Jul-Dec TS gradient between the western (10°S-10°N, 50-70°E) and eastern (10°S-0, 90-100°E) equatorial Indian Ocean in 1877 in both simulations. No blue dots to represent observations are included in (i-j) since TS from the GOGA simulations closely track the observed SSTs that are used as boundary conditions for the model. In the box-whisker plots, the

Figure 1

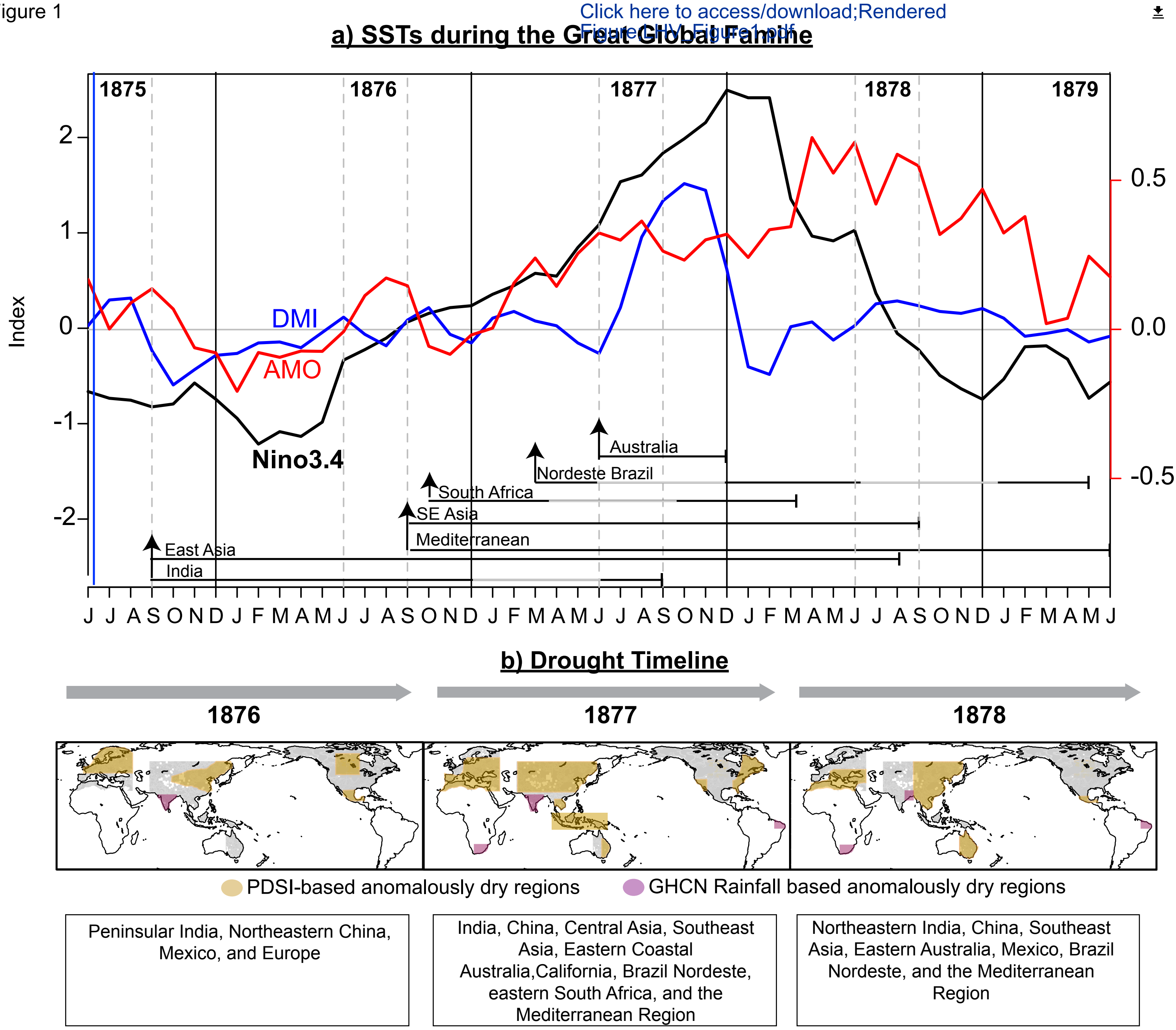

Figure 1. Drought extent and SST evolution: (a) Monthly evolution of the Niño3.4 Index, Atlantic Multidecadal Oscillation (AMO) Index, and the Indian Ocean Dipole Mode Index (DMI) during the Global Famine of 1876-1878. The approximate beginning and duration of dry conditions in major regions based on PDSI values (<-1.0) or seasonal rainfall anomalies (<-1.0σ), or a combination of both, are indicated by arrows and lines. Since PDSI from the regional drought atlases is annually resolved, the duration of drought in the regions identified based on PDSI (i.e East Asia, North Africa, and SE Asia) are indicated for the 12-month period ending in the reconstruction season (i.e Sep-Aug for MADA, OWDA, and NADA). Grey lines indicate seasons outside the main rainy seasons. (b) Extent of dry conditions (colored regions) during each of the three years based on negative PDSI (<-1.0; brown) or low rainfall (<-1.0σ; pink) conditions. Grey areas highlight the extent of the drought atlases and white areas indicate absence of data. To identify the characteristics of dry conditions, PDSI values are from the regional drought atlases and rainfall anomalies (relative to 1901-1950) are from the GHCN database. Note: the dry regions depicted in panels (b) are approximate and for illustrative purposes. Some sub-regions within the broader area depicted here might have differing conditions.

Figure 2

Click here to access/download;Rendered Figure;LHV_Figure2_PDSI_revised.pdf

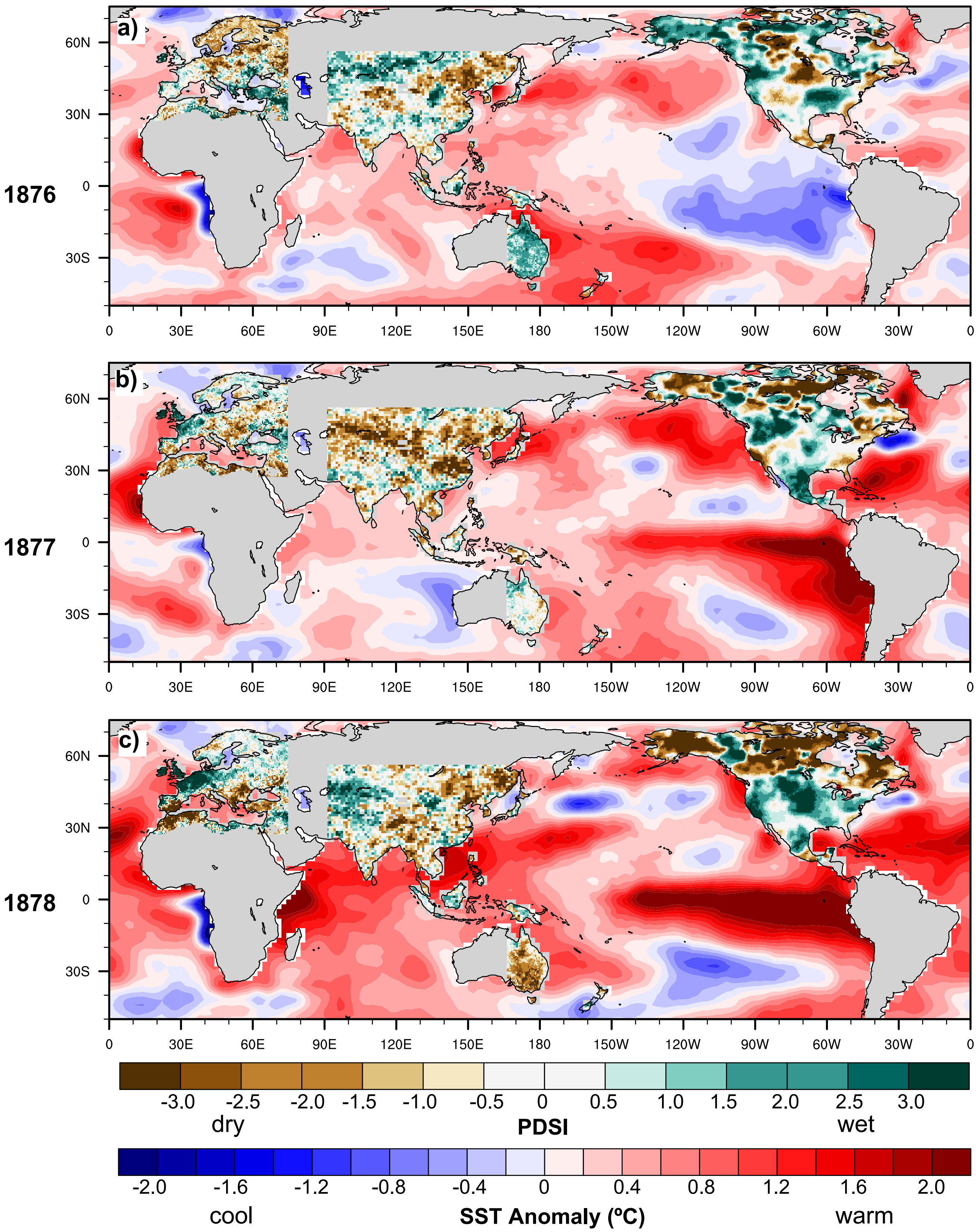

Figure 2. The Great Drought 1876-78: Sep-Aug (12-month) average sea-surface temperature (SST) anomalies during 1875-76, 1876-77 and 1877-78; and Palmer Drought Severity Index (PDSI) from the drought atlases for each of the three years. MADA, NADA, and OWDA provide June-August PDSI and ANZDA provides the December-February PDSI. Since PDSI integrates the moisture supply and demand over preceding seasons, we provide average detrended SST anomalies for the 12-month period from the preceding September to the concurrent August. SST anomalies are calculated relative to the 1901-1950 baseline period.

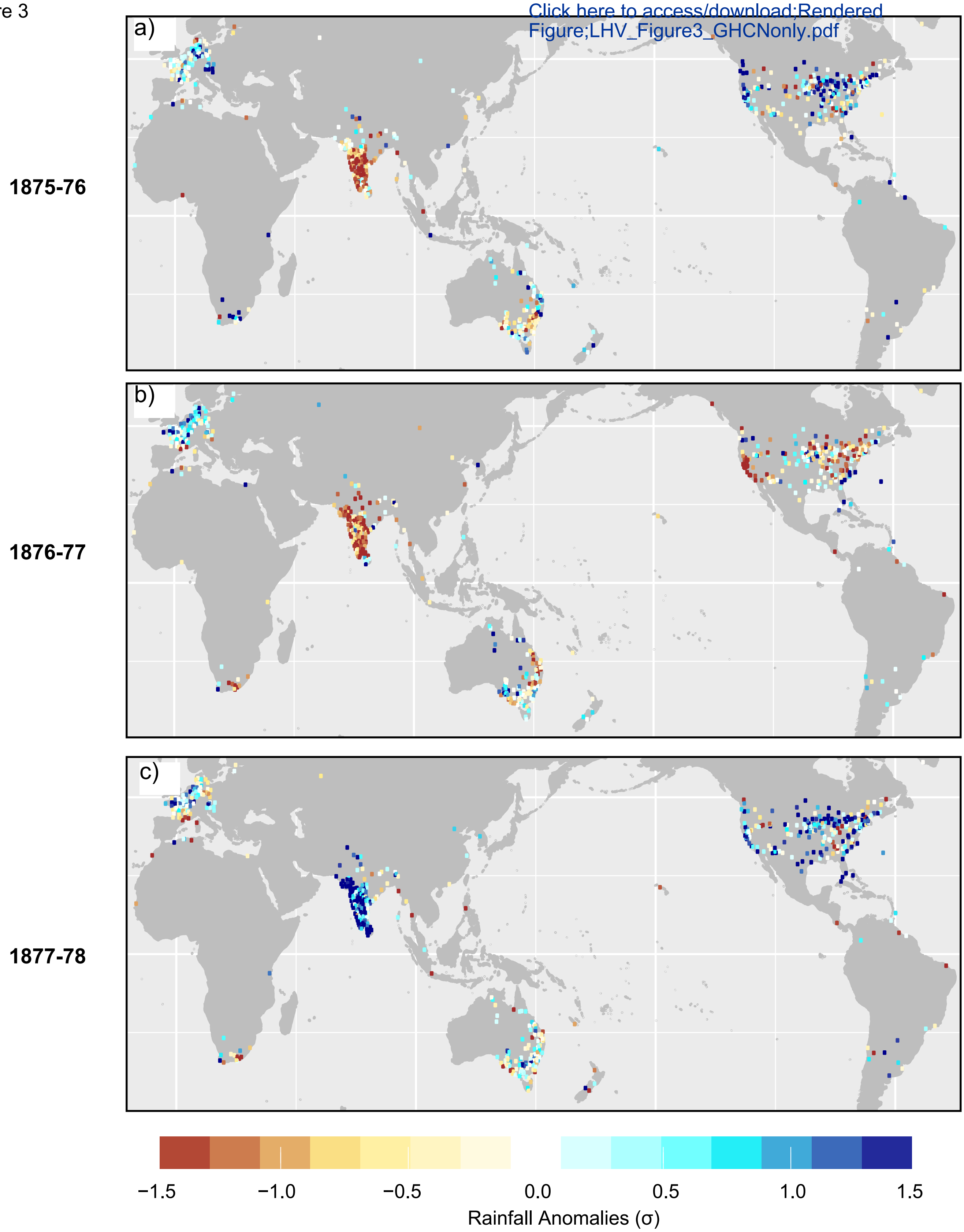

Figure 3. Global rainfall anomalies during the Great Drought: Standardized anomalies of 12-month (Sep-Aug) cumulative rainfall at available GHCN stations during the three periods: (a) 1875-76, (b) 1876-77, and (c) 1877-78. Anomalies are with reference to the 1901-1950 climatology.

Figure 4

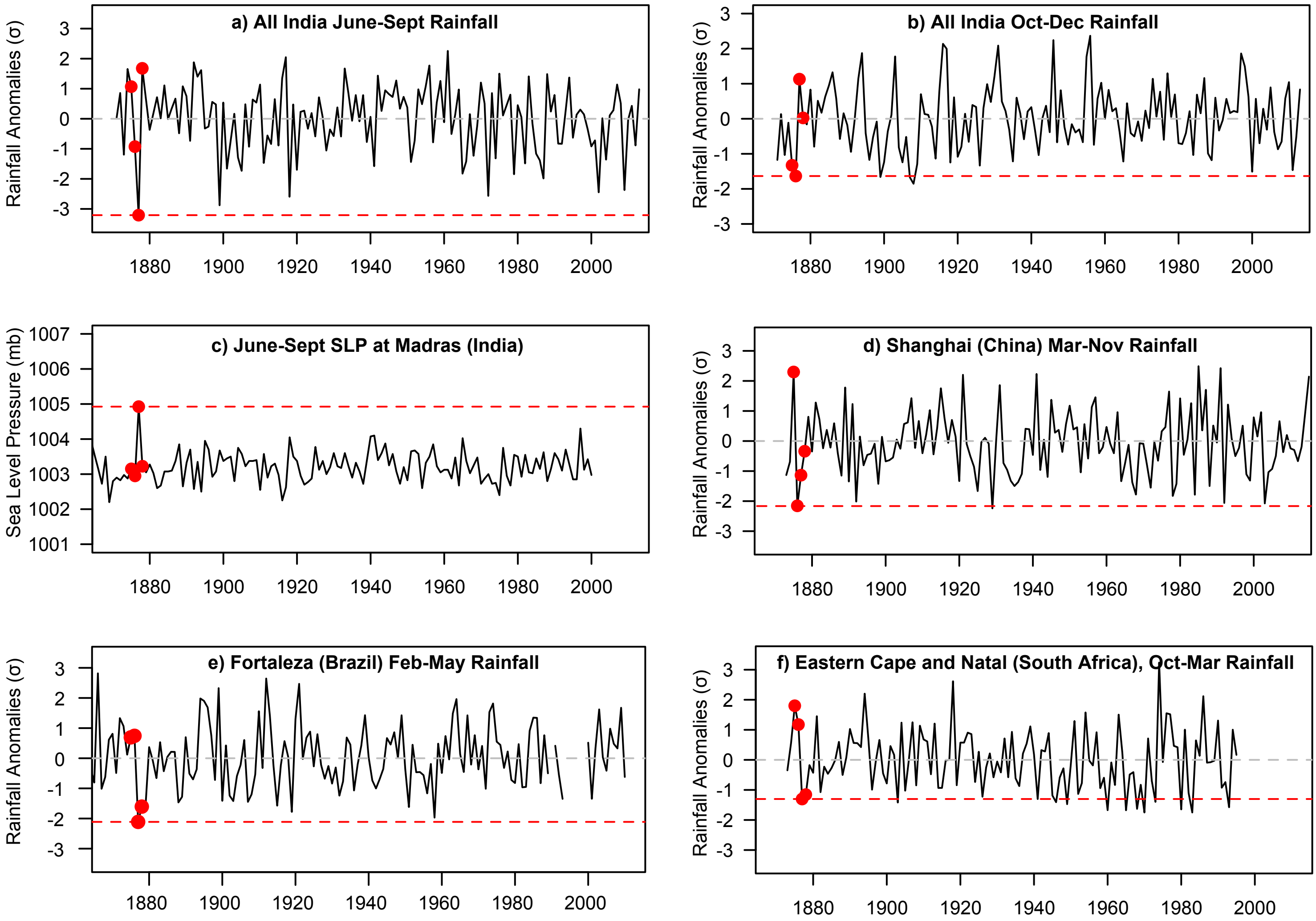

Figure 4. Severity of Rainfall Anomalies: Time series of (a) standardized anomalies of summer (Jun-Sep) monsoon rainfall for the All India region, (b) standardized anomalies of winter (Oct-Dec) monsoon rainfall for the All India region, (c) sea-level pressure at Madras, India, (d) standardized anomalies of Mar-Nov rainfall at Shanghai, China, (e) standardized anomalies of Feb-May rainfall at Fortaleza in the Brazil Nordeste, and (f) standardized anomalies of Oct-Mar rainfall in eastern South Africa (average of 6 stations in the Eastern Cape and KwaZulu-Natal provinces). The 4 red dots highlight years from 1875 to 1878, and the horizontal red line indicates the magnitude of the peak anomalies within this 4-year period for reference. The length of the Madras SLP record is limited by the length of the available timeseries and the South African rainfall timeseries is limited by the unavailability of data at multiple stations in the GHCN database post-1997. Rainfall for the 1997-1998 rainy seasons at Fortaleza are missing in the record. Gaps in any of the records represent missing values. Anomalies are calculated from the 1901-1950 baseline period.

Figure 5

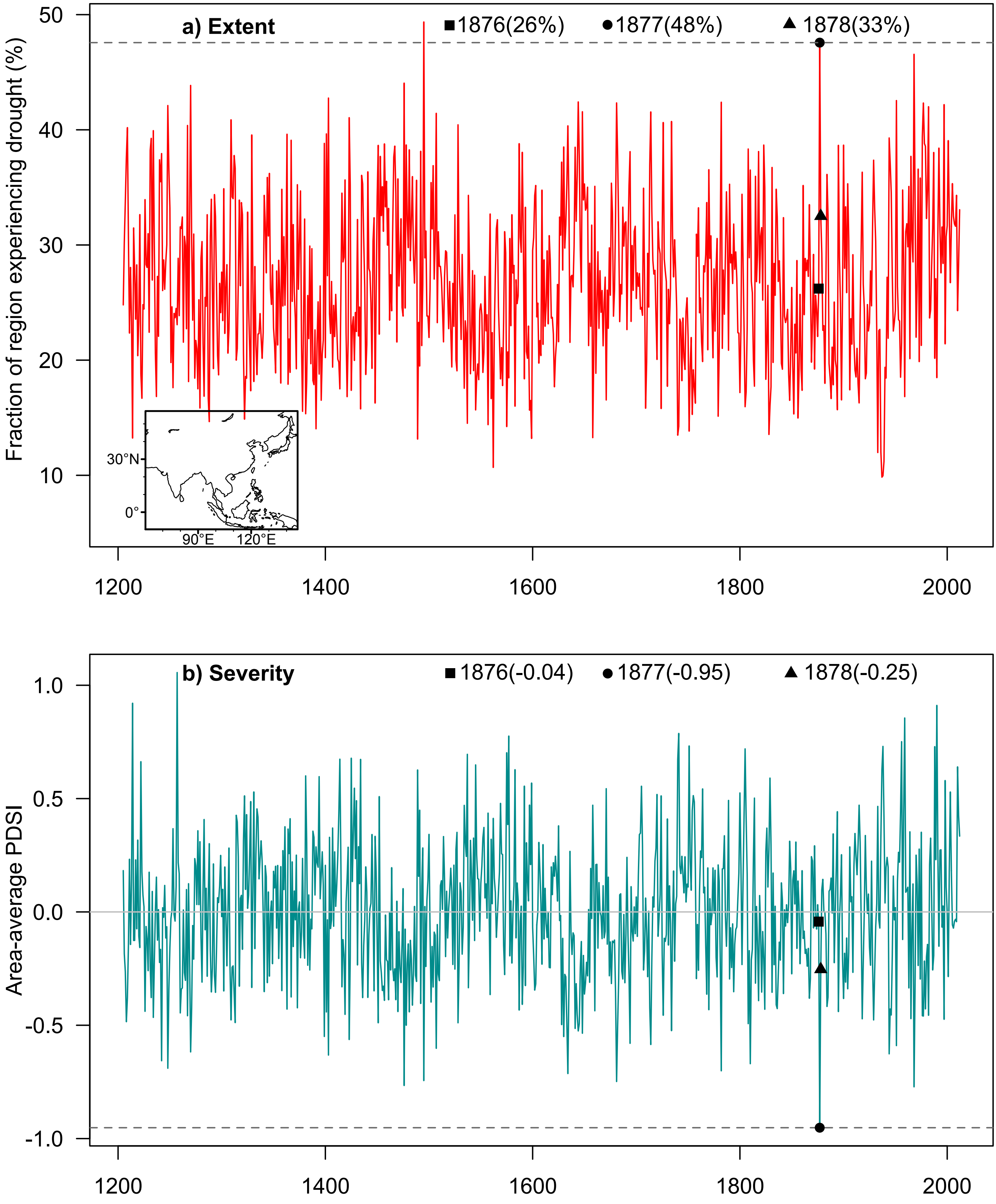

Figure 5. Monsoon Asia Drought Severity and Extent: Time series of (a) the fraction of the Monsoon Asia region (inset) experiencing drought (PDSI <-1.0), expressed as a percent, and (b) the area-weighted average PDSI across the region from 1205-2012. The drought severity and extent for each year of the drought is indicated in the corresponding panels. Dashed grey lines indicate the magnitude of these characteristics during the peak of the drought in 1877. The 1877 drought extent is the second highest and drought severity is the strongest since the early 1200s.

Figure 6

Click here to access/download;Rendered Figure;LHV_Figure6_india.pdf

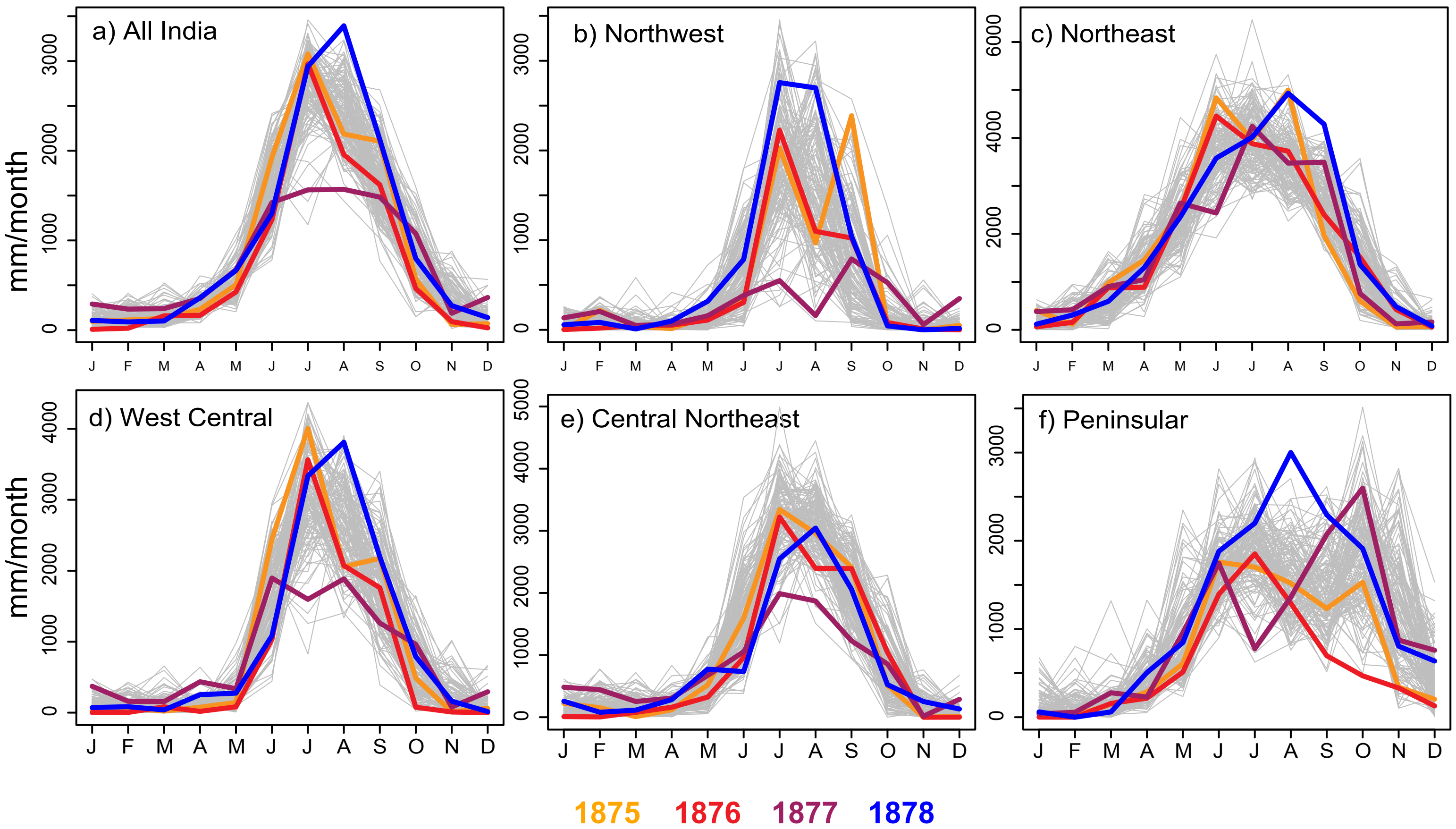

Figure 6. Temporal evolution of drought over India: Rainfall for the All India domain and 5 sub-regions defined by the Indian Institute of Tropical Meteorology (IITM) based on the similarity in their rainfall characteristics (refer Fig. 2 in Parthasarathy et al. (1995) or http://www.tropmet.res.in/IITM/region-maps.html). Colored lines highlight the evolution of drought across different regions between 1875 and 1878. Grey colors show all other years between 1870-2013.

Figure 7

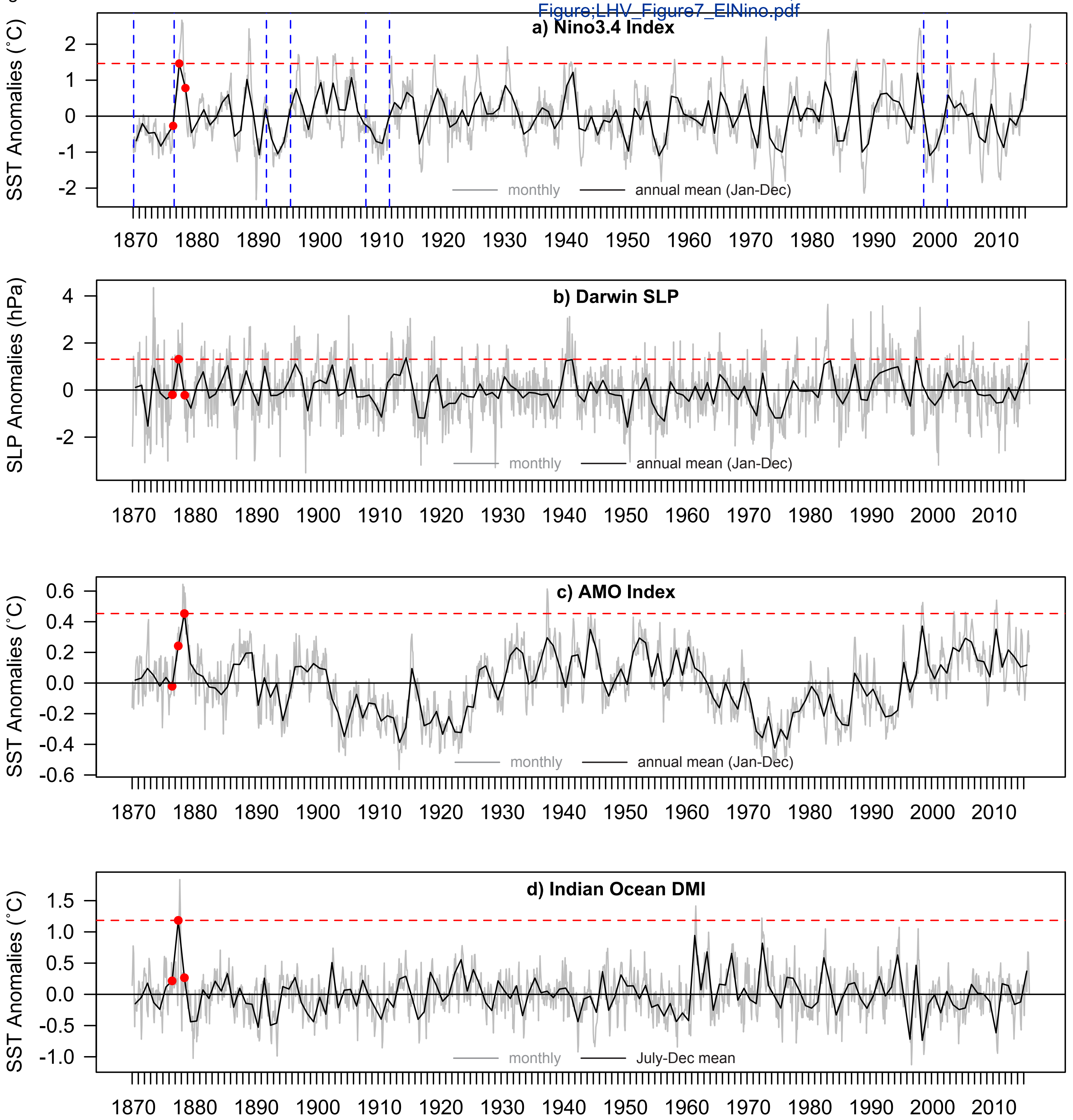

Figure 7. ENSO and SST features: Long-term de-trended time-series of the (a) Niño 3.4 Index, (b) Darwin sea-level pressure anomalies (hPa), (c) AMO Index, and (d) Indian Ocean Dipole Mode Index (DMI). Dashed red lines indicate the peak magnitude of the index between 1876-78. Vertical blue lines in panel (a) highlight the 4 longest prolonged cool periods in the equatorial Pacific, which are defined as consecutive months with Niño3.4 SST anomalies consistently below 0.2˚C. Anomalies are calculated from the 1901-1950 baseline period.

Figure 8

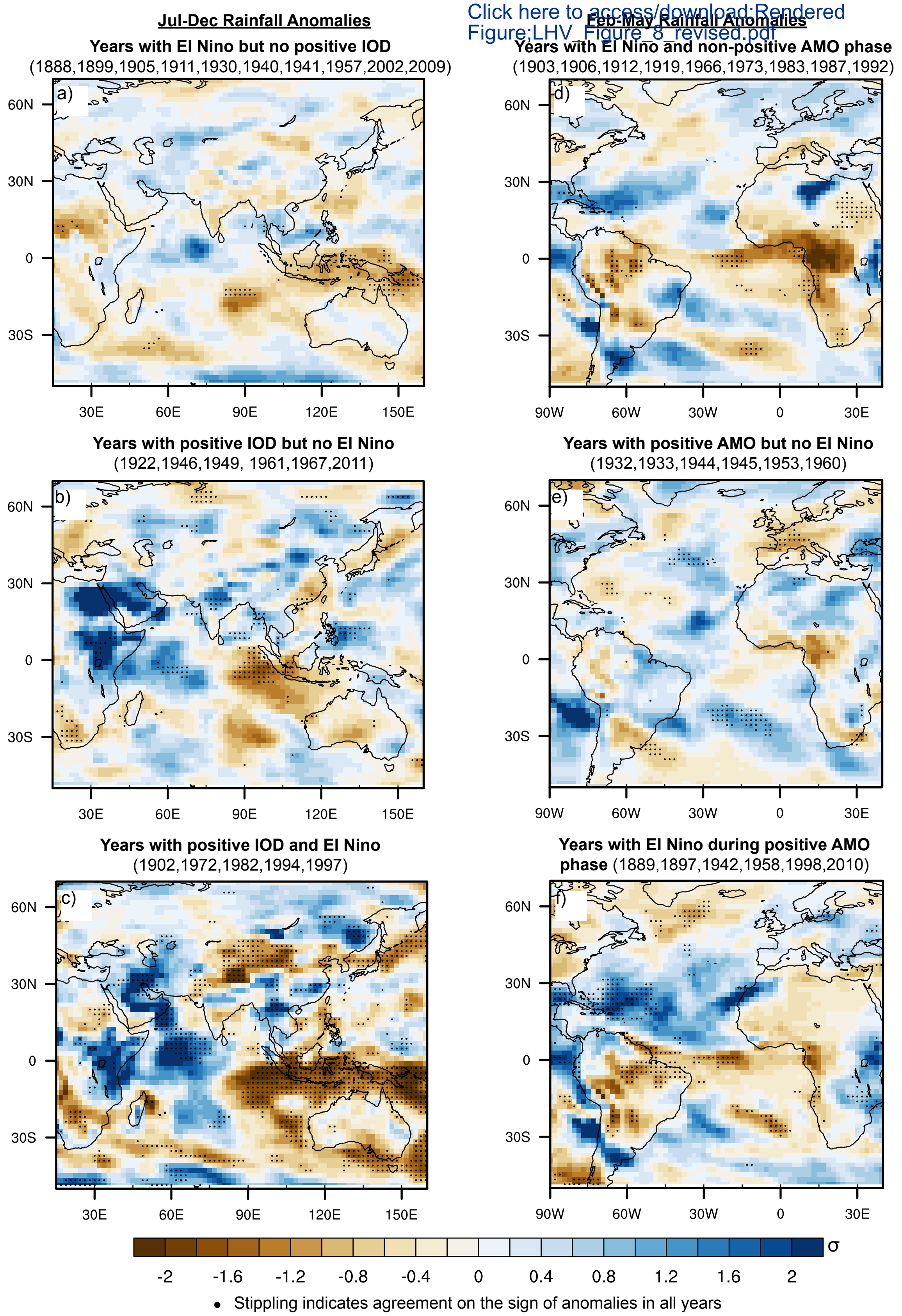

Figure 8. Influence of different ocean basins: Composite standardized rainfall anomalies for Jul-Dec from 20CR during (a) years with developing El Nino events without positive IOD events, (b) years with positive IOD events without concurrent El Nino events, and (c) years with positive IOD and developing El Nino events. Jul-Dec is selected to coincide with the cycle of positive IOD events. Composite average rainfall anomalies for Feb-May during (d) years with strong El Nino events during non-positive (neutral or negative) AMO events, (e) years with positive AMO events without El Nino events, and (f) years with strong El Nino events during positive AMO phases. Feb-May is selected to coincide with the peak rainy season over Nordeste Brazil and the peak AMO following a strong El Nino event. El Nino events are selected based on Nov-Mar Nino 3.4 index exceeding 1.0σ. (Note that years in the left column indicate years of developing El Nino events.). Positive AMO events are selected based on Feb-May AMO index exceeding 1.0σ. Positive IOD events are selected based on July-Dec DMI Index >1.0σ. Standardized rainfall anomalies are calculated based on the mean and standard deviation (σ) of the baseline period 1901-1950.

Figure 9

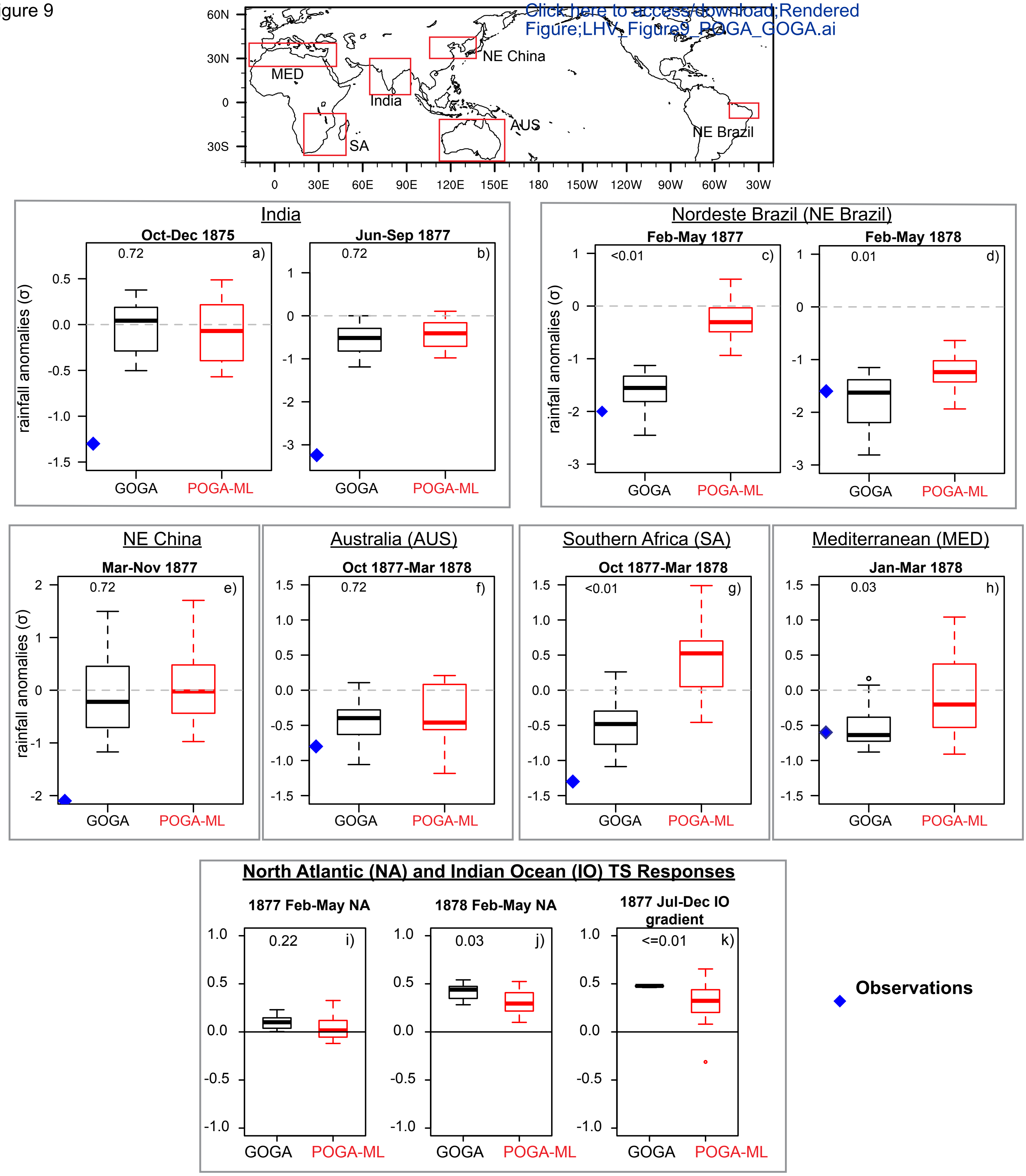

Figure 9. Role of Tropical Pacific versus Global Oceans: (a-h) Standardized rainfall anomalies in years associated with extreme deficits in different regions (see red boxes on map) from the 16-member ensemble of (black) GOGA and (red) POGA-ML simulations. For each region, seasons are chosen to coincide with the local main rainy seasons. Observed average rainfall anomalies for each region are indicated by blue diamonds. Average Feb-May North Atlantic (0-70°N, 80°W-0) surface temperature (TS) anomalies in (i) 1877 and (j) 1878, and average Jul-Dec TS gradient between the western (10°S-10°N, 50-70°E) and eastern (10°S-0, 90-100°E) equatorial Indian Ocean in 1877 in both simulations. No blue dots to represent observations are included in (i-j) since TS from the GOGA simulations closely track the observed SSTs that are used as boundary conditions for the model. In the box-whisker plots, the boxes represent the 25-75th percentiles and whiskers represent the 5-95th percentiles of the 16-member ensembles. Numbers in the top left indicate p-values from the Kolmogorov-Smirnov test for difference in distributions. Low p-values indicate that the distributions are significantly different. All anomalies are calculated relative to the 1901-1950 climatology.

Figure 10

Click here to access/download;Rendered Figure;LHV_Figure10_SST_scatterplots.ai

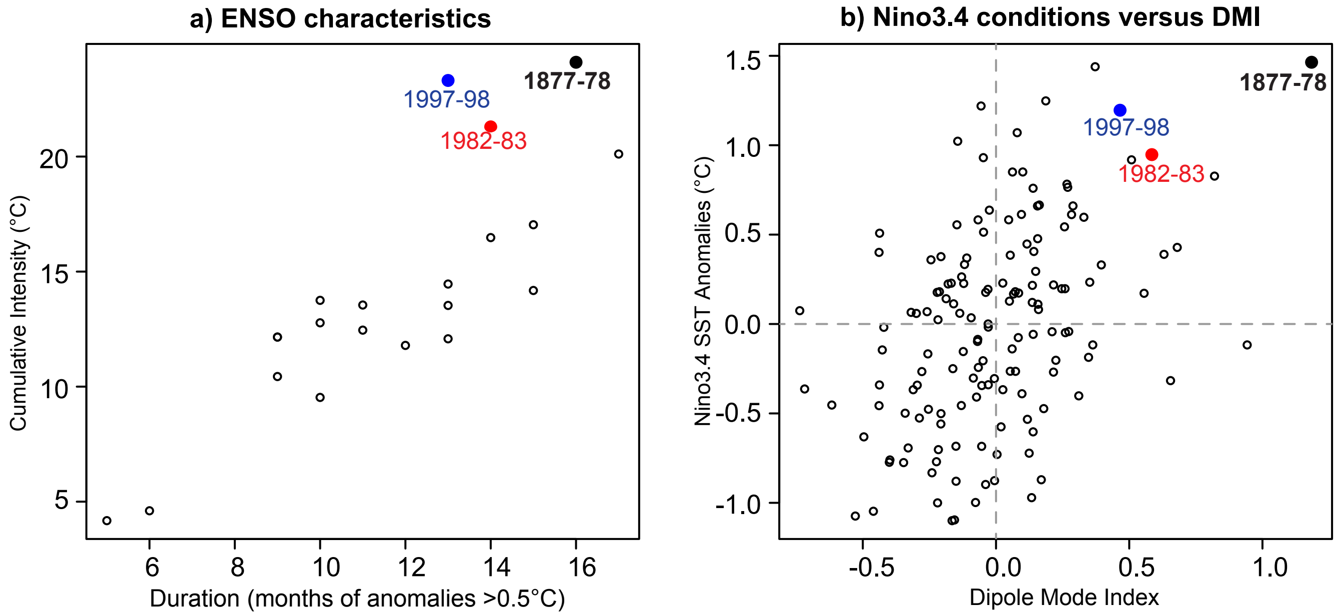

Figure 10. SST Characteristics: (a) Cumulative intensity and duration characteristics of all El-Niño events since 1870. Cumulative intensity is calculated as the sum of the monthly temperature anomalies over the duration of the El-Niño event and duration is the number of consecutive months with Niño3.4 anomalies exceeding 0.5°C. (b) Comparison of the magnitude of the annual mean Niño3.4 SST anomalies and the Jul-Dec seasonal mean DMI for all years between 1870-2015.

Figure 11

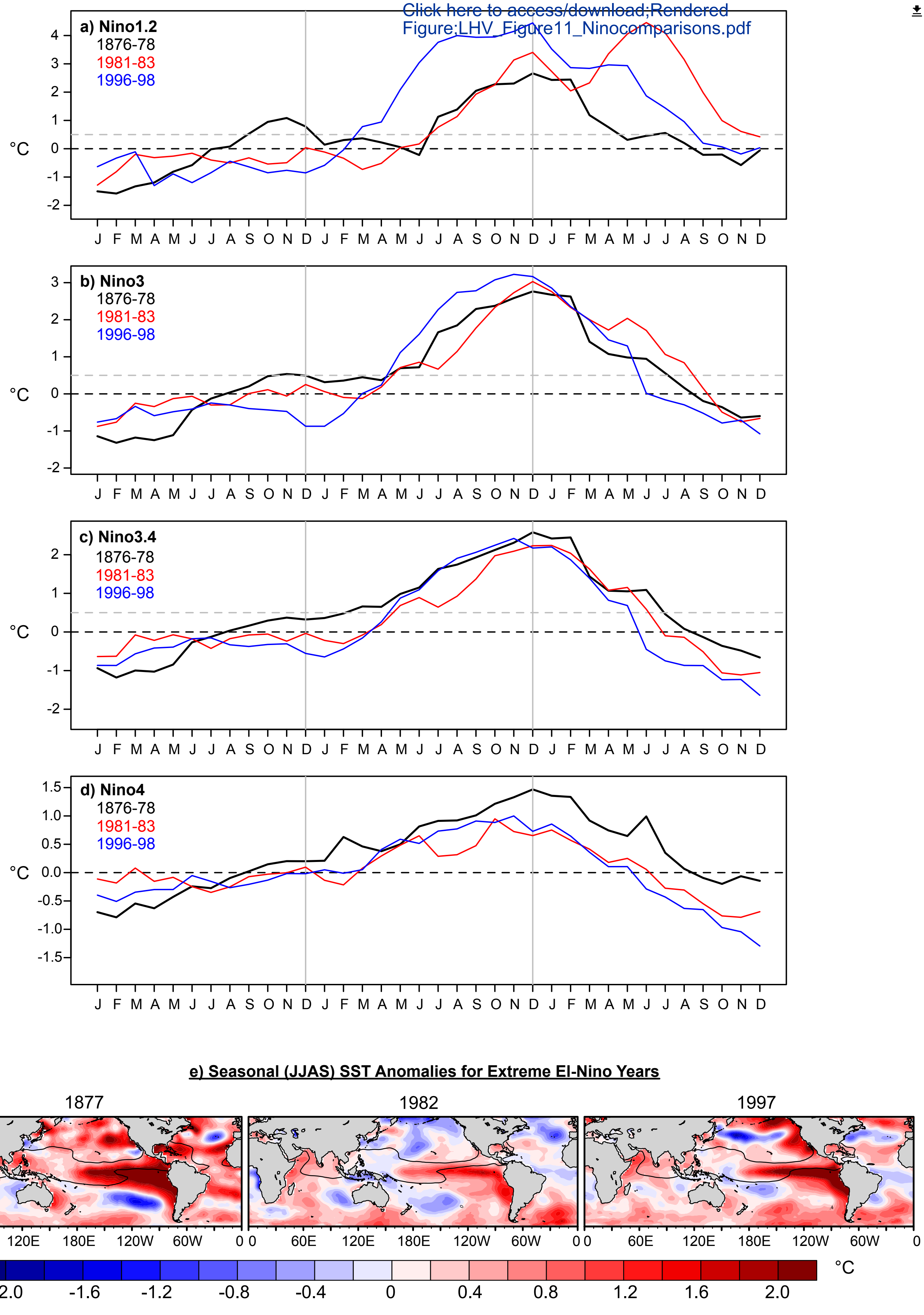

Figure 11. Features of Extreme El-Nino Events: Comparison of the temporal evolution of area-average, detrended SST anomalies (relative to 1901-1950 climatological mean) over the (a) Nino1.2, (b) Nino3, (c) Nino3.4, and (d) Nino 4 regions, during the 3 most extreme El-Ninos events - 1877-78, 1982-83, and 1997-98. (e) Global SST anomalies during the monsoon season (June - September) in these three years. The black contour line indicates the 28°C isotherm.

Figure 12

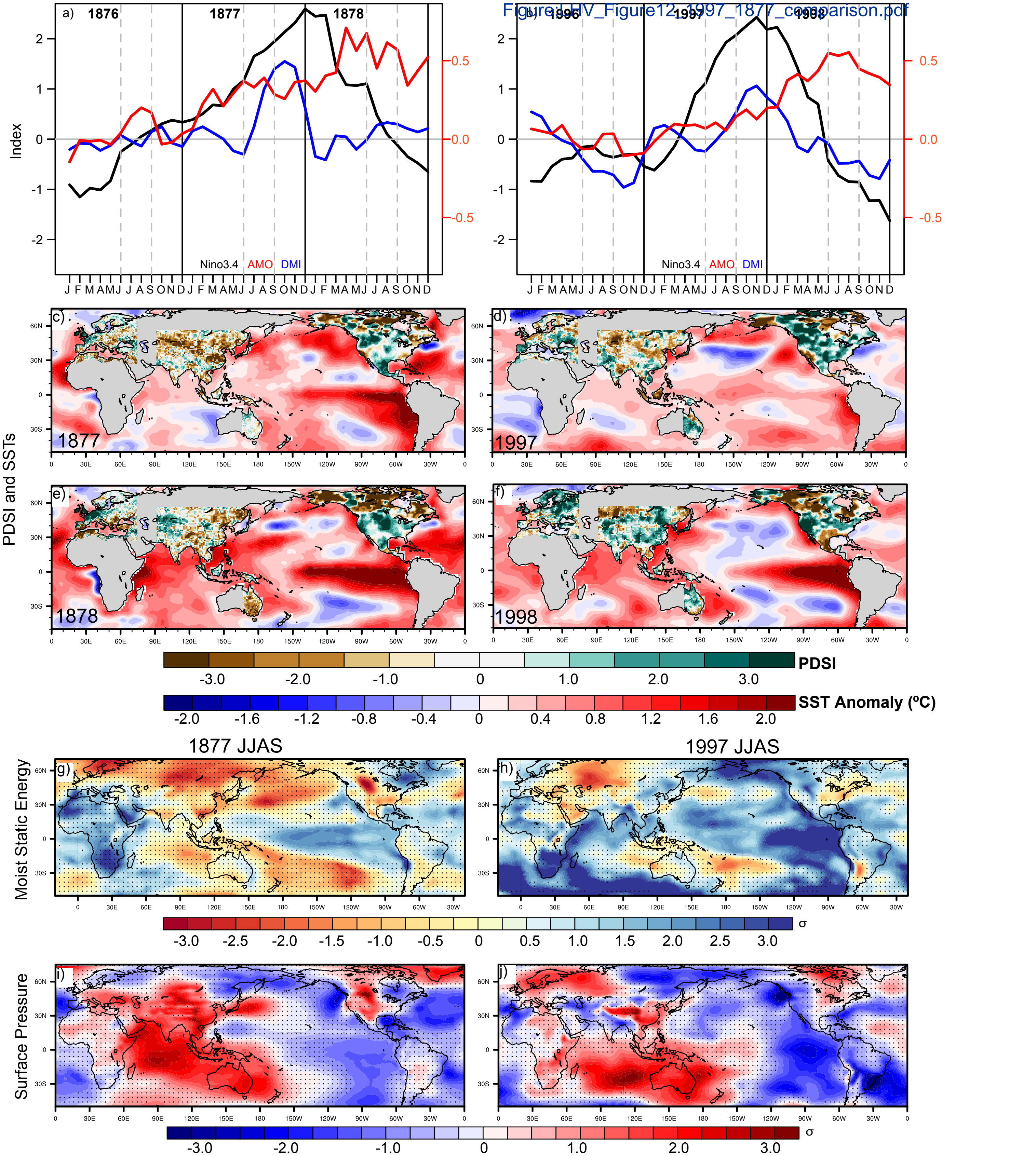

Figure 12. Comparison of 1877-78 and 1997-98 El Nino events: (a,b) Evolution of Nino3.4, AMO and IOD indices over the duration of each event, (c-f) PDSI and 12-month (September-August) average, detrended SST anomalies during the developing and decaying years of the El Ninos. (g,h) Moist static energy and (i,j) surface pressure anomalies for the summer monsoon season. Standardized anomalies are calculated using the mean and standard deviation of the 1901-1950 baseline period. Dots represent regions where anomalies are not significant. Significance is calculated based on the spread ($\pm 1\sigma_E$) of a variable in each season exceeding its spread ($\pm 1\sigma_E$) over the climatological period, where σ_E is the standard deviation between the 56 ensemble members of 20CR averaged to the seasonal-scale.